# Parametric analysis of core-noise from a realistic gas-turbine combustor for cruise and take-off conditions

Changxiao Shao [a], Davy Brouzet [a,*], Nicholas Rock [b], Matthias Ihme [a]

[a] *Department of Mechanical Engineering, Stanford University, Stanford, 94305, CA, USA*
[b] *Spectral Energies, LLC, BeaverCreek, OH, 45430, USA*

## ARTICLE INFO

## ABSTRACT

Combustion noise from a realistic gas-turbine combustor geometry is investigated parametrically using a hybrid simulation framework that combines large-eddy simulation and a linearized Euler formulation. The effect of operating conditions on the relative noise-source contributions arising from direct and indirect noise is examined by considering take-off and cruise conditions. To quantify the predictions of the combustion flow field, comparisons with available experimental data for velocity and spray droplet diameter are performed. Analysis of combustion dynamics shows that tonal combustion noise from a thermoacoustic instability is present at both operating conditions, which is consistent with experimental data. The unsteady combustion and dilution are the main sources for the fluctuations of pressure, temperature and mixture composition at the combustor exit. While the thermo-chemical properties do not significantly change between the two operating conditions, the simulation results show that the level of unsteadiness in the flow field is significantly higher for the take-off condition. This leads to an overall increase in the noise emissions by up to 20 dB at take-off compared to the cruise condition. Indirect noise arising from compositional inhomogeneities is found to exceed the entropy noise for both operating conditions. Phase cancellation between composition noise and temperature-induced noise is shown to result in an overall reduction of the indirect combustion-noise emissions.

## 1. Introduction

Commercial aircraft will continue to transport our society for decades to come. However, aircraft noise is one of the major issues because it adversely affects human's physiological and psychological health [1] and constrains air traffic growth [2]. Main contributors to aircraft noise arise from airframe and engine noise [3]. Airframe noise is generated by the trailing edge, landing gear and wings. In contrast, engine noise refers to the noise generated by the fan, in the engine core (compressor, combustor, and turbine), and in the jet exhaust. The present paper is concerned with the core-noise contributions associated with the combustor.

The relative contribution of engine-core noise draws more attention for modern engines. Specifically, in order to reduce emissions of greenhouse-gases and nitrous oxides ($NO_x$), advanced lean combustion technologies are employed [4]. However, these combustion concepts are prone to generate higher noise emissions due to the unsteady turbulent environment [5–7], especially at low frequencies [8]. In contrast, fan noise has largely been reduced by improving the fan-blade design. Similarly, jet noise was reduced by increasing the bypass ratio as well as improving the acoustic liners and nozzle design [3,9].

While many different acoustic sources might be present in a reacting environment [10], engine-core noise typically consists of two main distinct mechanisms, namely direct and indirect combustion noise [3, 7,11]. Direct combustion noise describes the transmission of pressure fluctuations originating from unsteady heat release in the combustion chamber [11]. The sound generated by direct combustion noise is transmitted to the downstream components and eventually propagates to the far-field. In contrast, indirect combustion noise is caused by the advection of vortices and entropy variations caused by temperature hot-spots as they are accelerated through the downstream turbine and nozzle [12]. More recently, contributions from mixture inhomogeneities were identified as an additional source of indirect combustion noise [3]. Theoretical analysis indicated that compositional noise can interact and even exceed indirect combustion noise that arises from temperature inhomogeneities [3,13]. The relative contributions of these noise-source mechanisms are dependent on the operating conditions, engine type, and interaction with other unsteady processes.

To investigate the relative contribution of direct and indirect combustion noise, several experiments have been conducted. With relevance to the analysis of indirect noise, Bake et al. [14] conducted

---

measurements in an entropy wave generator to examine entropy noise mechanisms, showing that indirect sources are several orders of magnitude larger than direct noise. More recently, Rolland et al. [15] performed measurements in a carefully designed entropy wave generator rig to quantify contributions from direct noise, entropy noise, and compositional noise, showing that experimental measurements for indirect noise are well described by theory.

To theoretically examine core noise, acoustic analogies have been developed for characterizing direct noise and jet-exhaust noise. Different methods have been proposed for modeling indirect noise, which include the compact nozzle theory [12,16], the effective nozzle length method [17,18], expansion methods [19,20], and non-linear analysis [21]. By extending the compact nozzle theory to multi-component gas mixtures, it was shown that compositional noise can exceed entropy noise for fuel-lean conditions and supercritical nozzle flows [13]. This implies that compositional noise should require consideration with the implementation of low-emission combustors.

Apart from experimental and theoretical investigations, multidimensional numerical simulations have been employed to investigate core noise [3]. Leyko et al. [22] compared direct and indirect noise mechanisms in a model combustor and found that indirect noise is small for laboratory experiments but increases for more realistic aeronautical engines. By using large-eddy simulations (LES), Papadogiannis et al. [23] examined the generation of entropy noise in a high-pressure turbine stage and found that the upstream entropy noise reduces due to the choked turbine nozzle guide vane. O'Brien et al. [24] employed a hybrid modeling approach to predict the far-field radiation of core noise from a model combustor that consists of a combustion chamber, turbine, and nozzle. Livebardon et al. [25] combined LES and actuator disk theory to predict combustion noise in a helicopter engine, confirming the importance of indirect combustion noise. Magri et al. [26] numerically calculated the indirect noise for finite-nozzle Helmholtz numbers and confirmed that compositional noise can exceed direct and entropy noise contributions in a choked nozzle and for lean mixtures.

Despite these studies on combustion noise, the relative contributions of direct and indirect noise to the overall core-noise radiation are not fully understood. This is especially true when considering compositional noise, which has been subject to less scrutiny than entropy-induced noise. To this end, we present a hybrid simulation framework for enabling noise-predictions in early engine-design analysis. This hybrid modeling approach combines LES for the prediction of the unsteady turbulent combustion with a linearized Euler formulation for the prediction of the noise generation through the downstream nozzle. The objectives are two-fold; (1) to demonstrate the applicability of the hybrid formulation by considering a realistic gas-turbine combustor application and (2) to examine the effect of the operating conditions on the noise emissions. We extend the scope of previous work [27] by performing a parametric study of a realistic gas-turbine combustor at thermo-acoustically unstable cruise and take-off conditions. We also demonstrate the utility in obtaining representative data for low-order modeling analysis. The experimental configuration and operating conditions are presented in Section 2. The mathematical model is presented in Section 3. Results are discussed in Section 4 and conclusions are provided in Section 5.

## 2. Experimental configuration and operating conditions

The referee combustor rig that is considered in this study was designed to reproduce features of a realistic rich-quench-lean (RQL) gas-turbine combustor [28,29]. A schematic of this combustor is shown in Fig. 1. The combustor consists of four components; namely the pressure plenum, the injector, the combustion chamber and the outlet plenum. The injector consists of an inner radial swirler and two outer axial swirlers that supply air to the combustion chamber. Fuel is supplied through a pressure-swirl atomizer. The combustion chamber has a

**Table 1**
Properties of Jet-A fuel at 322 K used in the present study; $W$: molecular weight, $\mu_l$: dynamic viscosity, H/C: hydrogen to carbon ratio, $\Delta h_f^0$: lower heating value, DCN: derived cetane number.

| Composition (mass fraction [%]) | | | | |
| --- | --- | --- | --- | --- |
| Aromatics | *iso*-Paraffins | *n*-Paraffins | Cycloparaffins | Alkenes |
| 18.66 | 29.45 | 20.03 | 31.86 | <0.001 |
| $W$ [kg/kmol] | $\mu_l$ [mPa s] | $\Delta h_f^0$ [MJ/kg] | H/C | DCN |
| 159 | 1.17 | 43.1 | 1.90 | 48.3 |

constant width of 110 mm in the primary and secondary combustion regions, and progressively reduces in the dilution zone until the exhaust, which is located 290 mm from the combustor inlet plane as shown in Fig. 1-(c). The upper and lower walls of the combustor consist of multi-perforated plates that supply air from the pressure plenum to the combustion chamber. These are modeled in the LES as homogeneous flows through the effusive boundaries. To ensure conservation of mass, a constant negative mass flow is imposed in the outer region, while a positive flow is imposed on the inner walls. There are two rows of dilution holes in the upper and lower walls of the chamber: the first row that consists of three dilution holes on each side is located 45 mm downstream of the inlet plane, and the second row consisting of four dilution holes on the lower and upper sides is 132 mm downstream of the inlet plane. The combustion chamber is housed inside a pressure plenum. Further geometric details are provided in [28,30,31].

Considering the nominal operating point from the National Jet Fuel Combustion Program (NJFCP), the impact of the fuel on the lean blowout (LBO) limit has been studied in prior numerical works [30,32,33]. These LBO cases have also been extensively studied experimentally [28, 31]. In the present work, we extend from this nominal configuration and consider cruise and take-off conditions at higher fuel mass flow rates that are representative of more typical engine operating conditions.

The present study considers a conventional petroleum-derived Jet-A fuel (Cat-A2, POSF10325). The thermo-physico-chemical properties for this fuel are obtained from studies conducted by the NJFCP [29]. These properties, evaluated at a temperature of 322 K (corresponding to the injection condition), are listed in Table 1. The properties of the liquid fuel are dependent on the temperature, and effects of pressure on the properties were found to be negligible [34,35].

To parametrically examine the effect of the operating conditions on the noise emission, we consider two different operating points corresponding to a cruise condition and a take-off condition. For the cruise condition, the engine is assumed to operate at an altitude of 10,600 m and at a flight Mach number of 0.8. At this condition, the combustor is operated at approximately 20% of the maximum take-off power [36,37]. The conditions for this operation point are identical to that considered in the experimental study of the same combustor rig [38]. The combustor is supplied with air at a temperature of $394\pm2.5$ K and the total air mass flow rate is $391.4 \pm 6.9$ g/s. The pressure inside the combustion chamber is $2.07 \pm 0.01$ atm. The fuel is supplied through a pressure-swirl atomizer at $322 \pm 2.3$ K at a mass flow rate of 4.0 g/s with an uncertainty of 0.15%. The overall equivalence ratio is $\phi_g = 0.15$.

The take-off operating point is specified by considering sea-level conditions. To determine the other parameters for the take-off condition, i.e. mass flow rates and combustor pressure, we are considering a typical high-bypass ratio turbo-fan engine that consists of a fan, compressor, combustor, turbine and nozzle. The thrust generated is determined as [39]

$$F = \dot{m}_C \left[ (1 + f)U_9 + \beta U_{19} - (1 + \beta)U_0 \right] + A_9 \left( p_9 - p_0 \right) + A_{19} \left( p_{1e} - p_0 \right) ,$$

(1)

where $\dot{m}_C$ is the air mass flow rate through the core, $f_r$ is the fuel–air ratio, $\beta$ is the bypass ratio, $U_9$ and $U_{19}$ are the core exit velocity
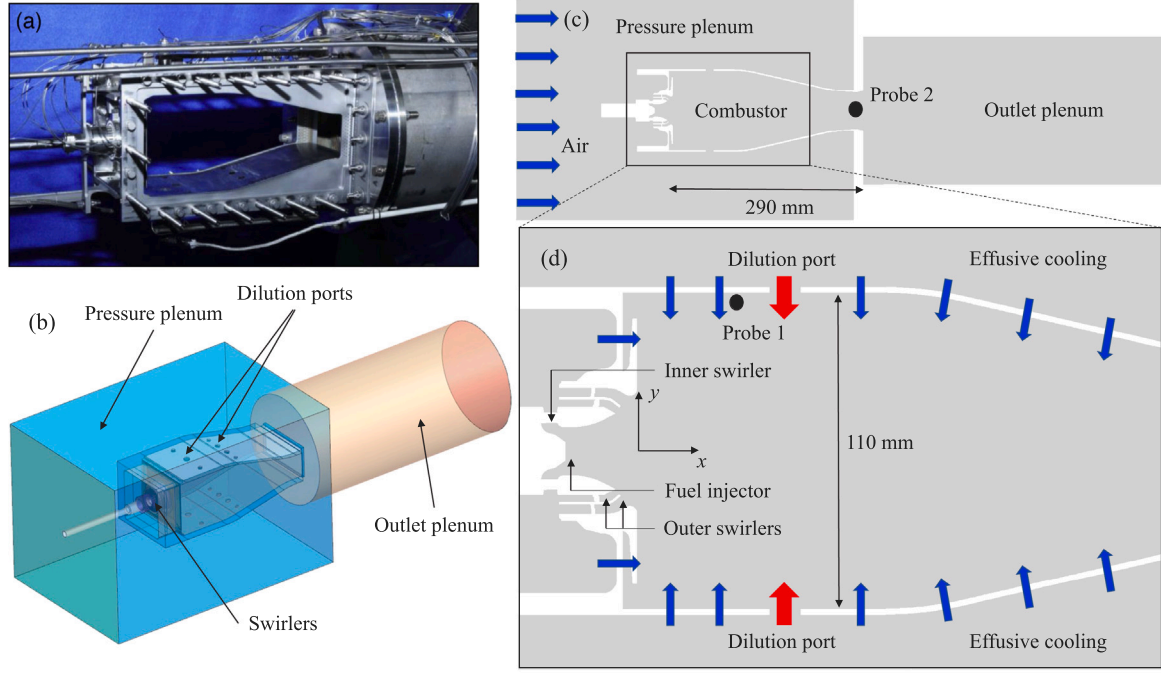
**Fig. 1.** (a) Disassembled referee-rig combustor and (b) CAD of the geometry. (c–d) Schematic diagram (*x*-*y* plane) of the referee combustor rig, where the arrows represent different streams entering the combustor. The probe is used to monitor the combustor exit conditions.

and fan exit velocity, $U_0$ is the flight velocity, $p_9$ and $p_0$ are the static pressure at the jet nozzle and the ambient pressure, and $A_9$ and $A_{19}$ are the core and fan cross sections, respectively. Assuming a perfectly expanded nozzle flow, the pressure thrust in Eq. (1) is neglected, and the operating parameters for the take-off condition are then determined from an ideal Brayton-cycle analysis [39]. To anchor the take-off operating point in relation to the cruise condition, we prescribe the fan pressure ratio and bypass ratio from a CFM56 high-bypass ratio turbofan engine [40], i.e., $\pi_f = 1.28$ and $\beta = 6.6$. All other parameters for the combustor pressure, fuel mass-flow rate, and equivalence ratio are then computed subject to prescribed conditions for flight Mach number $M_0$, ambient temperature $T_0$, ratio of specific heats $\gamma$, heat capacity $c_p$, lower heating value $\Delta h_f^0$, temperature at the combustor exit $T_{t4}$, compressor pressure ratio $\pi_c$, fan pressure ratio $\pi_f$, and bypass ratio $\beta$. Details on the governing equations and solution procedure for determining the operating conditions are provided in Appendix A. The temperature at the combustor exit is determined iteratively to obtain compressor pressure ratios for the cruise and take-off conditions. The operating parameters for both conditions are summarized in Table 2.

## 3. Mathematical model

### 3.1. Hybrid method

A hybrid modeling framework is employed to predict the generation and transmission of engine-core noise. In this hybrid approach, a compressible reacting multiphase LES solver is used to compute the turbulent combustion. The unsteady flow-field at the combustor exit is then extracted from the LES and prescribed as inflow boundary condition to a reduced-order nozzle simulation using the linearized Euler equations (LEE). The nozzle is represented by a converging–diverging supersonic nozzle.

### 3.2. Combustor simulation

The three-dimensional computational domain considered in the LES calculation includes the pressure plenum, the combustion chamber

**Table 2**
Operating parameters for the cruise and take-off conditions.

| Parameters | Description | Cruise | Take-off |
|---|---|---|---|
| $M_0$ [–] | Flight Mach number | 0.8 | 0.0 |
| $\pi_c$ [–] | Compressor pressure ratio | 5.71 | 9.56 |
| $\tau_c$ [–] | Compressor temperature ratio | 1.645 | 1.906 |
| $T_{t3}$ [K] | Combustor inlet temperature | 394.0 | 549.3 |
| $T_{t4}$ [K] | Combustor exit temperature | 837.4 | 1349.5 |
| $p_t$ [atm] | Pressure in combustor | 2.07 | 10.35 |
| $V_9$ [m/s] | Core nozzle exit velocity | 464.76 | 695.33 |
| $M_9$ [–] | Core nozzle exit Mach number | 1.09 | 1.31 |
| $F/\dot{m}_0$ [N/(kg/s)] | Specific thrust | 87.91 | 269.52 |
| $\dot{m}_C$ [g/s] | Air mass flow rate through core | 391.4 | 765.2 |
| $\dot{m}_f$ [g/s] | Fuel mass flow rate | 4.0 | 14.2 |
| $\phi_g$ [–] | Global equivalence ratio | 0.15 | 0.28 |
| $f_r$ [–] | Fuel–air ratio | 0.01 | 0.01856 |
| $TSFC$ [mg/s/N] | Thrust specific fuel consumption | 14.97 | 9.06 |
| $F$ [N] | Thrust | 261.22 | 1567.32 |
| $T_f$ [K] | Injection fuel temperature | 322.0 | 322.0 |
| $d_{SMD}$ [μm] | Sauter mean diameter | 56.0 | 14.5 |

and the outlet plenum (see Fig. 1). The domain is discretized using a block-structured mesh with 18.3 million hexahedral elements. In the near-wall, swirler and free-shear layer regions, the mesh resolution is finer with a characteristic size of 0.15 mm. Numerical simulations are performed using an unstructured and fully compressible solver [41–43]. The instantaneous Favre-averaged conservation equations for mass, momentum and energy are solved with a second-order accurate spatial discretization scheme. Operator splitting is employed for time integration, in which the non-stiff advection–diffusion operators are solved using a third-order accurate strong-stability preserving Runge–Kutta scheme [44]. To integrate the stiff chemical source terms, a semi-implicit Rosenbrock–Krylov scheme is used, having 4th-order accuracy and linear cost with respect to the number of species [45]. Turbulent subgrid stresses are modeled using the Vreman model [46]. No-slip wall boundary conditions are used and effusive cooling is modeled through a homogeneous approach, where the effusive gas-phase velocity is determined from the experimentally measured mass flow rates [30].

Adiabatic wall boundaries are used in the simulation since the convective heat transfer to the walls is expected to have negligible effect on the flame due to the multiperforated plates used around the combustor.

The flamelet/progress-variable (FPV) model [47,48] is employed to model the combustion process in which the thermochemical properties are parameterized as a function of filtered mixture fraction $\widetilde{Z}$, filtered progress variable $\widetilde{C}$, and mixture fraction variance $\widetilde{Z''^2}$. The gas-phase system of Favre-filtered conservation equations for mass, momentum and energy takes the following form:

$$\partial_t \bar{\rho} + \nabla \cdot (\overline{\rho \boldsymbol{u}}) = -\{\dot{m}_d\} \ , \tag{2a}$$

$$\partial_t (\overline{\rho \boldsymbol{u}}) + \nabla \cdot (\overline{\rho \boldsymbol{u} \boldsymbol{u}}) = -\nabla \bar{p} + \nabla \cdot (\bar{\boldsymbol{\tau}} + \boldsymbol{\tau}_t) \ , \tag{2b}$$

$$\partial_t (\bar{\rho} \widetilde{E}) + \nabla \cdot (\overline{\rho \boldsymbol{u}} \widetilde{E}) = -\nabla \cdot \left[ \left( \frac{\bar{\lambda}}{c_p} + \frac{\mu_t}{Pr_t} \right) \nabla \widetilde{h} - \widetilde{\boldsymbol{u}} \bar{p} + \widetilde{\boldsymbol{u}} (\bar{\boldsymbol{\tau}} + \boldsymbol{\tau}_t) \right] \ , \tag{2c}$$

$$\partial_t (\bar{\rho} \widetilde{Z}) + \nabla \cdot (\overline{\rho \boldsymbol{u}} \widetilde{Z}) = -\nabla \cdot \left( \bar{\boldsymbol{j}}_Z + \boldsymbol{j}_{Z,t} \right) + \dot{\overline{S}}_Z \ , \tag{2d}$$

$$\partial_t (\bar{\rho} \widetilde{C}) + \nabla \cdot (\overline{\rho \boldsymbol{u}} \widetilde{C}) = -\nabla \cdot \left( \bar{\boldsymbol{j}}_C + \boldsymbol{j}_{C,t} \right) + \bar{\rho} \widetilde{\dot{\omega}}_C \ , \tag{2e}$$

$$\partial_t (\bar{\rho} \widetilde{Z''^2}) + \nabla \cdot (\overline{\rho \boldsymbol{u}} \widetilde{Z''^2}) = -\nabla \cdot \left( \bar{\boldsymbol{j}}_{\widetilde{Z''^2}} + \boldsymbol{j}_{\widetilde{Z''^2},t} \right) \ , \tag{2f}$$

where $\rho$ is the density, $\boldsymbol{u}$ is the velocity vector, $p$ is the pressure, $\boldsymbol{\tau}$ is the viscous stress tensor, $\boldsymbol{\tau}_t$ is the sub-grid scale stress, and $\mu_t$ is the turbulent eddy viscosity which is modeled with the Vreman approach. The thermal conductivity is denoted by $\lambda$, $c_p$ is the heat capacity, $Pr_t$ is the Prandtl number and $h$ is the enthalpy. The molecular and turbulent diffusive fluxes for the scalar $\phi$ are denoted as $\bar{\boldsymbol{j}}_\phi = -\bar{\rho} \widetilde{D}_\phi \nabla \widetilde{\phi}$ and $\boldsymbol{j}_{\phi,t} = -\mu_t / Sc_t \nabla \widetilde{\phi}$, respectively, where $D_\phi$ is the diffusion coefficient and $Sc_t$ is the turbulent Schmidt number. The volume-average of the evaporation rate over all droplets in the computational cell is denoted by $\{\dot{m}_d\}$. Finally, $\dot{\overline{S}}_Z$ and $\widetilde{\dot{\omega}}_C$ are the evaporation source terms of the mixture fraction and the chemical source term of the progress variable, respectively.

In the present work, the thermochemical state is described from the solution of steady laminar non-premixed flamelets that are solved in composition space [49]. The combustion chemistry model of the Cat-A2 fuel is described by a HyChem mechanism [30,50], which consists of 113 species and 790 reactions. This model is developed following a hybrid approach [50], where fuel pyrolysis is described by seven lumped reaction steps and primary products include $H_2$, $CH_4$, $C_2H_4$, $C_3H_6$, $1\text{-}C_4H_8$, $i\text{-}C_4H_8$, $C_6H_6$ and $C_6H_5CH_3$. The progress variable is defined as $C = Y_{CO_2} + Y_{CO} + Y_{H_2O} + Y_{H_2}$ [51].

To consider the cooling effect due to evaporation of the liquid phase on the flamelet solution, an effective gaseous fuel temperature [52] is computed as $T_{f,g} = T_{f,l} - \Delta h_v (T_{evap}) / c_l (T_{evap})$, where $\Delta h_v$ is the latent heat of evaporation and $c_l$ is the specific heat capacity of the liquid fuel. For the conditions considered in this work, $T_{f,g}$ = 191 K. To generate the flamelet solutions for the cruise and take-off conditions, effects of pressure are considered by computing different flamelet tables. The flamelet solutions are calculated using a counterflow diffusion flame configuration, and the maximum temperature curves as a function of the scalar dissipation rate are reported in Fig. 2, showing differences in the extinction limit between the cruise and take-off conditions. Differences in the maximum flamelet temperature are a consequence of the different oxidizer environment.

A Lagrangian particle tracking approach is employed to describe the spray, and the liquid droplet motion is represented by the Basset–Boussinesq–Oseen equation [53]. Secondary break-up (SBU) of spray droplets is modeled using a stochastic approach [54] where the droplet size is assumed to be time dependent with a given initial size distribution. The governing equations for the spray phase and the breakup model can be found in Refs. [53,54]. The critical Weber number, $We_{d,c} = \rho_g |\boldsymbol{u}_s|^2 r_d / \sigma_l$, which determines the droplet breakup is set to a value of 6.0, where $\rho_g$ is the gas density, $\boldsymbol{u}_s$ is the local droplet slip velocity, $r_d$ is the droplet radius, and $\sigma_l$ is the surface tension. The

droplet-size distribution at the injector inlet is prescribed using the following correlation [55]:

$$d_{SMD} = 2.25 \sigma_l^{0.25} \mu_l^{0.25} \dot{m}_f^{0.25} \Delta p^{-0.5} \rho_{air}^{-0.25} \ , \tag{3}$$

where SMD is the Sauter mean diameter, $\mu_l$ is the fuel viscosity, $\dot{m}_f$ is the fuel mass flow rate, $\Delta p$ is the pressure drop across the fuel injector nozzle and $\rho_{air}$ is the air density. For the cruise condition, $\Delta p$ is available from experimental data and the flow number of the injector can be computed as $FN = \dot{m}_f / \sqrt{\Delta p} = 1.18 \times 10^{-3}$ gs$^{-1}$Pa$^{-0.5}$. Assuming a constant $FN$, the pressure drop at the take-off condition is then evaluated. Eq. (3) has a functional dependence on the fuel mass flow rate, so that $d_{SMD}$ attains different values for the take-off and cruise conditions. Based on Eq. (3), the SMD is determined to be 14.5 μm for the take-off condition and 56.0 μm for the cruise condition. The droplet size distribution is then prescribed from a Rosin–Rammler distribution and provided as boundary condition at the fuel injector,

$$P(d; \bar{d}, n) = \left( \frac{d}{\bar{d}} \right)^n \frac{n}{d} \exp \left\{ - \left( \frac{d}{\bar{d}} \right)^n \right\} \quad \text{with} \quad \bar{d} = d_{SMD} \frac{\Gamma(2/n+1)}{\Gamma(3/n+1)} \ , \tag{4}$$

where $\bar{d}$ is the characteristic diameter, $\Gamma$ is the gamma function, and $n$ is the spread parameter, which is kept constant at 2.25 [30]. The resulting distributions for both conditions are illustrated in Fig. 3.

### 3.3. Coupling of combustor exit and nozzle flow

This section summarizes the coupling method between the LES method and Linear Euler model [27]. The combustor exit, having a rectangular cross-section, is connected to the nozzle inlet. We introduce a Cartesian coordinate system, where the combustor exit lies on the $y$-$z$ plane and the $x$-axis is aligned with the nozzle center line. The combustor exit-flow was well mixed along the spanwise direction. This allows us to reduce the flow through the nozzle to a two-dimensional planar problem so that the nozzle inlet condition only depends on $y$ and $t$. We decompose the flow variable $q$ at the exit plane into mean (denoted by $\langle \cdot \rangle$) and fluctuating (denoted by a prime) quantities:

$$q(y, t) = \langle q \rangle (y) + q'(y, t) \ , \tag{5}$$

where $q = \{u, p, s, Z\}$ and $s$ is the entropy. The fluctuating quantities are expressed as:

$$q'(y, t) = \int A_q(y, f) \exp\{-i(2\pi f t + \theta_q)\} df \ , \tag{6}$$

where $A_q$, $f$, and $\theta_q$ are the amplitude, frequency, and phase, respectively.

In the present study, we are concerned with examining the component of fluctuations at the dominant frequency, $f_c$. To this end, we first apply a band-pass filter to the combustor-exit data to extract the corresponding frequency component. Subsequently, Proper Orthogonal Decomposition (POD) is applied to the filtered data, and the first spatial POD mode is used to prescribe the spatial dependence of $A_q$. POD is a modal decomposition technique that can extract coherent structures from spatio-temporal dynamic data [56]. POD of a variable $q'(y, t)$ is given as:

$$q'(y, t) = \sum_{i=1}^{N} \psi_i(y) \phi_i(t) \ , \tag{7}$$

where $\psi_i(y)$ and $\phi_i(t)$ are the $i$th spatial and temporal POD modes, respectively. The first spatial POD mode $\psi_1(y)$ contains the most energy and typically represents the coherent spatial variation of $q'$.
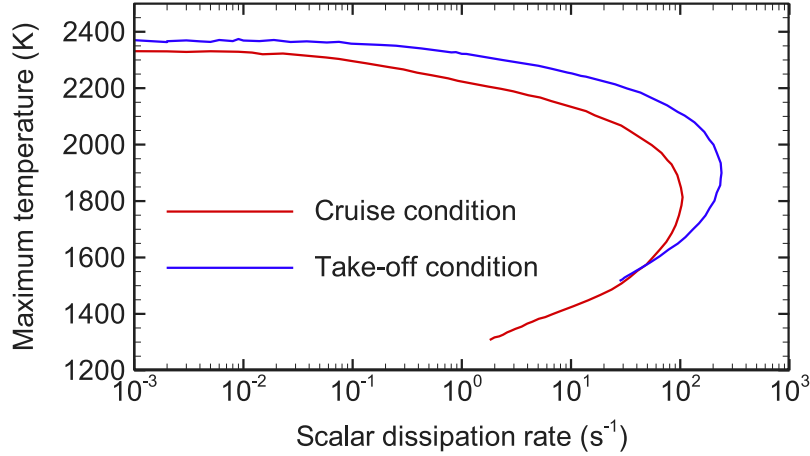
**Fig. 2.** Comparison of maximum temperature in a counterflow diffusion flame configuration as a function of the scalar dissipation rate for the cruise and take-off conditions.
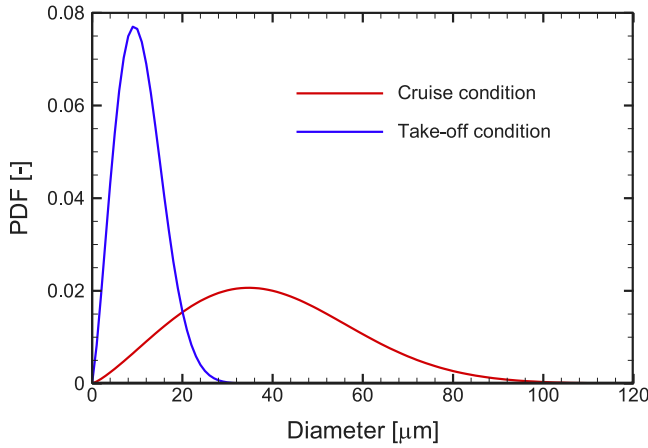


**Fig. 3.** Rosin–Rammler droplet-size distribution used as spray boundary condition.

### 3.4. Nozzle-flow simulations

The acoustic transmission through the nozzle is described by the solution of the linearized Euler equations. Substituting the decomposed mean and fluctuating variables into the Euler equations and collecting the first-order terms of the fluctuating quantities, the LEE can be obtained as

$$\partial_t s' + \langle u \rangle \cdot \nabla s' = -u' \cdot \nabla \langle s \rangle , \tag{8a}$$

$$\partial_t u' + \langle u \rangle \cdot \nabla u' = -u' \cdot \nabla \langle u \rangle - \frac{1}{\langle \rho \rangle} \nabla p'$$
$$- \left( \frac{p'}{\gamma \langle p \rangle} - \frac{s'}{c_p} - \Psi Z' \right) \langle u \rangle \cdot \nabla \langle u \rangle , \tag{8b}$$

$$\partial_t p' + \langle u \rangle \cdot \nabla p' = -u' \cdot \nabla \langle p \rangle - \gamma \left( \langle p \rangle \nabla \cdot u' + p' \nabla \cdot \langle u \rangle \right) , \tag{8c}$$

$$\partial_t Z' + \langle u \rangle \nabla Z' = -u' \cdot \nabla \langle Z \rangle , \tag{8d}$$

where $\Psi$ is the chemical potential function. The governing equations are non-dimensionalized using the inlet conditions.

Spatial derivatives in the governing equations are evaluated using an explicit, eleven-point, wavenumber optimized finite difference scheme [57]. Temporal discretization is performed using an explicit fourth-order Runge–Kutta method with a constant timestep. An explicit and optimized filter [57] is used for the numerical stabilization at every time step. No-penetration boundary conditions are prescribed at the walls. Solution variables, obtained from the upstream combustion LES, are prescribed at the nozzle inlet. An absorbing buffer zone [58] is applied in the nozzle-upstream region, and the damping term has a quadratic distribution within the buffer zone with a damping constant of 0.5. Characteristic and non-reflecting boundary conditions [59] are applied at the outflow.

To simplify the nozzle flow simulation, the following assumptions are invoked: frozen chemistry in the nozzle, isentropic flow, and linear-velocity nozzle. We use the linear nozzle proposed by Duran and Moreau [19] to represent the converging–diverging supersonic nozzle. The nozzle geometry is designed so that the axial velocity increases linearly along the nozzle axis. With this condition, the nozzle shape is constructed by invoking the isentropic flow assumption:

$$\frac{A}{A_*} = \frac{1}{M} \left[ \left( \frac{2}{\gamma+1} \right) \left( 1 + \frac{\gamma-1}{2} M^2 \right) \right]^{\frac{\gamma+1}{2(\gamma-1)}} , \tag{9}$$

where $A_*$ is the critical nozzle area and $M$ is the Mach number. The Mach number in this nozzle is calculated as a function of the axial coordinate [19]. The base state $\langle q \rangle$ is obtained from the upstream LES results and is constructed along the nozzle by using the isentropic relation. It is noted that the base state of the mixture fraction is constant since frozen chemistry is considered.

So far, contributions from compositional noise has been widely neglected in the literature so that only indirect noise from temperature inhomogeneities was considered. Temperature and compositional perturbations are correlated but each source provides a physically different contribution to the overall indirect noise. The generation of compositional noise introduces the chemical potential function, $\Psi$, as shown in Eq. (8b). This quantity introduces a direct dependency on the chemical potential $\mu_i$ and is calculated as a function of the chemical composition and partial Gibbs free energy [3]:

$$\Psi = \frac{1}{c_p T} \sum_i \left( \frac{\mu_i}{W_i} - \Delta h_i^0 \right) \frac{dY_i}{dZ} = \frac{1}{c_p T} \sum_i^{N_s} g_i \frac{\partial Y_i}{\partial Z} , \tag{10}$$

where $\Delta h_i^0$ is the formation enthalpy of the $i$th species, $W_i$ is the molecular weight of the $i$th species, $T$ is the temperature, $Y_i$ is the mass fraction of the $i$th species, and $g_i$ is the specific Gibbs energy of the $i$th species. The derivative $\partial_Z Y_i$ is evaluated from the solution of a steady laminar flamelet at a scalar dissipation rate $\chi_{st} = 1$ s$^{-1}$, which corresponds to the condition at the combustor exit.

The acoustic transmission is predicted in the form of a transfer function that compares the magnitude of an imposed disturbance at the nozzle inlet to the resulting disturbance at the nozzle outlet. In these studies, the transfer function is expressed in characteristic form for the downstream and upstream acoustic waves, advected entropy perturbations, and compositional perturbations,

$$\pi^\pm = \frac{1}{2} \left( \frac{p'}{\gamma \langle p \rangle} \pm \frac{u'}{\langle a \rangle} \right) , \tag{11a}$$
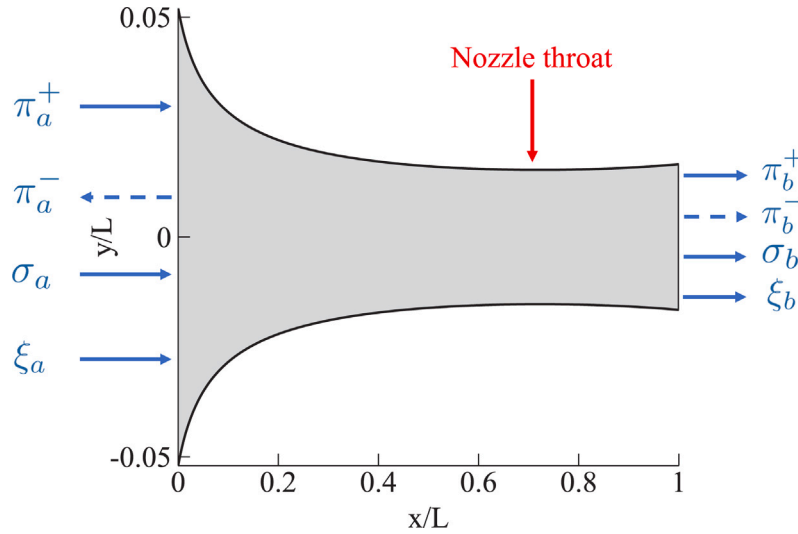
**Fig. 4.** Schematic diagram of downstream acoustic wave $\pi^+$, upstream acoustic wave $\pi^-$, entropy perturbation $\sigma$ and compositional perturbation $\xi$ along the nozzle.

$$\sigma = \frac{s'}{c_p}, \tag{11b}$$

$$\xi = Z'. \tag{11c}$$

To study independently the transmission of direct noise, and the generation of entropy noise and compositional noise, each perturbation modes is considered individually in the LEE-simulation. A schematic of these waves is illustrated in Fig. 4. Transverse velocity fluctuations are not considered and therefore vorticity noise cannot be predicted by the current LEE model. To nondimensionalize the frequency, we introduce the Helmholtz number as $He = fL/a$, where $L = 0.5$ m is the nozzle length and $a$ is the speed of sound at the nozzle inlet. The details on the nozzle geometry are provided in Appendix B.

## 4. Results and discussion

In this section, we first examine the combustor dynamics before analyzing the combustion noise characteristics of the system.

### 4.1. Combustion analysis

*Comparison to experimental data.* As part of previous studies [27,30], we examined the accuracy of the LES combustion simulations and investigated dependencies of the modeling results on the computational setup, mesh resolution, and subgrid closures. By considering the nominal NJFCP condition, quantitative comparisons with measurements for mass-flow splits, blow-out limits, droplet distribution, and chemiluminescence were performed. More recently, PIV measurements for the velocity field [60] were acquired and this data is used for additional comparison in Fig. 5. Results for both the streamwise and transverse velocity components agree well in the internal recirculation zone and the annular jet region. The spreading rate is also well captured by the LES. Two regions show significant discrepancies; the bulkhead flow at the top/bottom left in Fig. 5(a–b) and the dilution holes region. None of these inlets were seeded with particles in the PIV, leading to a greater uncertainty in the measurements [60].

Fig. 6 shows the droplet size distribution obtained in the LES at the nominal operating condition and at a location downstream the SBU region but upstream the primary combustion zone. Comparing this distribution to the polydispersed fuel injection performed in the simulation (Fig. 3), it can be seen that the mean droplet size has significantly decreased due to SBU. Fig. 6 also shows the droplet size distribution from measurements, reported in Ref. [30]. While small-size droplets are more frequent in the experiments, the most probable

droplet diameter $D_{mp}$ is similar between experiments and simulations, which confirms the utility and validity of the SBU model. The maximum distribution value and corresponding droplet diameter differ by 30% and 10%, respectively. Furthermore, the experimental data was taken at cold conditions [61]. Some discrepancies are therefore expected, especially for small droplets, as they would have fully evaporated once they reached the inlet plane. Further comparisons of spray velocity statistics can be found in Ref. [27].

*Thermo-acoustic instability characteristics.* We proceed by examining the instantaneous pressure signal at the combustor exit and the integrated heat release rate. The flame was shown to be acoustically compact in the simulated configuration [28]. The pressure is recorded at a probe that is located at the center of the combustor exit, and results are shown in Fig. 7. These results show that the pressure exhibits strong harmonic fluctuations at the dominant frequencies of $f_c = 254$ Hz for the cruise condition and $f_c = 451$ Hz for the take-off condition. It is noted that the dominant frequency for the cruise condition agrees well with experimentally reported measurements that identified a tonal mode ($f_{exp} = 260$ Hz) [28] at the same operating condition. We also display the temporal evolution of the global heat release rate over a time period of approximately six oscillation cycles in Fig. 7, showing that pressure and heat release are mostly in-phase for the cruise condition while having approximately a phase difference of 90° for the take-off condition.

We further examine the modal shape along the axial distance through the combustor for both conditions in Fig. 8. The pressure fluctuation is normalized by the mean chamber pressure and the mode shape is extracted at the peak frequency for the cruise condition (254 Hz) and take-off condition (451 Hz). The root-mean-square (RMS) pressure value at $x = 0.035$ m equals 3100 Pa at the cruise condition, which agrees well with the experimental results (∼3500 Pa) reported by Monfort et al. [38]. Fig. 8 also shows that the modes are longitudinal for both conditions and pressure nodes are located at the combustor exit. Note that the plenum outlet in the simulation acts as a reflecting boundary, which mimics the pressure node of the first acoustic mode in the referee rig [38]. The same longitudinal mode is reported by the experiments for the cruise condition [38]. Fig. 8 also shows that different axial mode shapes develop for different operating conditions. Specifically, a quarter-wave that extends through the combustor and plenum is present for the cruise condition. For the take-off condition, however, the higher frequency of the instability leads to the excitation of a mode shape with an additional pressure node at the combustor exit ($x = 0.29$ m).
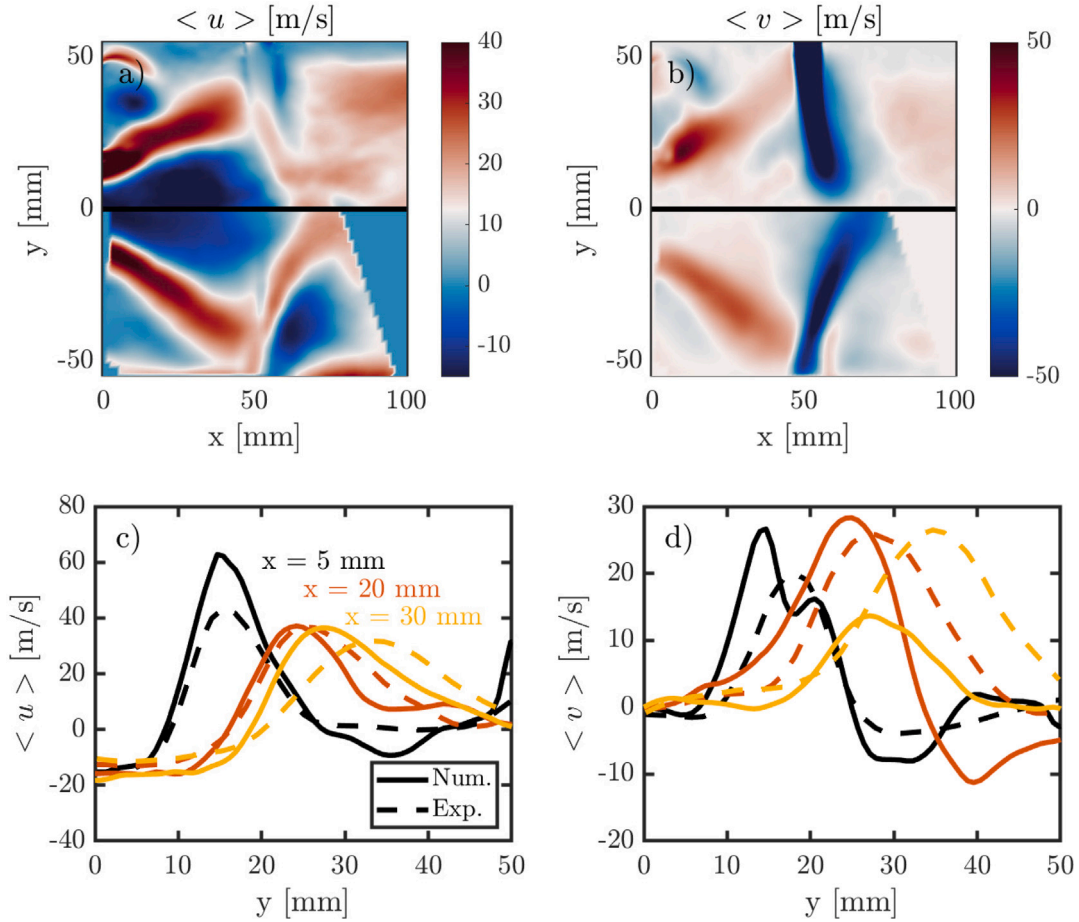
**Fig. 5.** Comparison between mean numerical results (upper sub-panels) and PIV measurements (lower sub-panels) of the (a) *x-y* centerplane streamwise velocity and (b) the *x-y* centerplane transverse velocity. Comparisons at different streamwise locations for (c) the streamwise velocity and (d) the transverse velocity. The effusive flow and dilution jets were not seeded with particles in the PIV measurements.
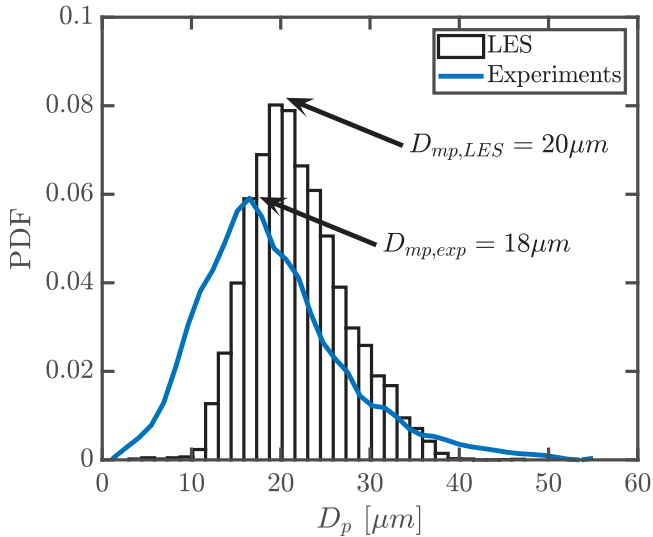


**Fig. 6.** Comparison of droplet size distribution between reacting numerical and cold-flow experimental results at the streamwise and radial locations $(x, r) = (0.0, 0.015)$ m.

*Instantaneous results.* Since temperature and mixture inhomogeneities at the combustor exit are the main mechanisms for the generation of indirect noise in the downstream nozzle, it is instructive to examine

the instantaneous reacting flow field inside the combustor. Figs. 9 and 10 illustrate the dynamics of the unsteady combustion during a thermoacoustic cycle, where $\delta_t$ is the cycle period determined by the characteristic frequency that is identified in Section 4.2 (Take-off: $\delta_t = 2.2$ ms; Cruise: $\delta_t = 4.0$ ms). For both operating points, the combustion is initially confined to the primary zone (Fig. 9(a)). At later time, the flame extends into the secondary combustion zone, resulting in the formation of isolated flame regions that advect downstream where they mix with the surrounding flow from the secondary dilution and effusive cooling. This is consistent with the findings by Sattelmayer [62], who showed that entropy spots are subjected to strong dispersion due to the highly turbulent nature of the flow in realistic combustors. Temperature fluctuations of the order of 100 K are however still observed at the combustor exit. Their acoustic contribution when accelerated through a nozzle will be investigated in Section 4.2.

Instantaneous mixture fraction fields, defined using Bilger's formulation [63], are shown in Fig. 10. It can be seen that for the take-off condition the mixing process extends into the downstream region, which is a consequence of the higher mass flow rate and the richer environment. The injection of air through the effusive cooling and the dilution holes in the secondary combustion zone enhances the mixing and significantly reduces the mixture fraction fluctuations. Dassé et al. [64] have performed LES to analyze the acoustic response of liners and found that Howe's model [65] performs well. Given that a thermo-acoustic instability is present, it is sensible to assess the acoustic response of the effusive flow using this model. The flow through the effusion holes is approximately 60 m/s and their diameter is close to 2 mm. At the characteristic frequencies of interest, velocity fluctuations
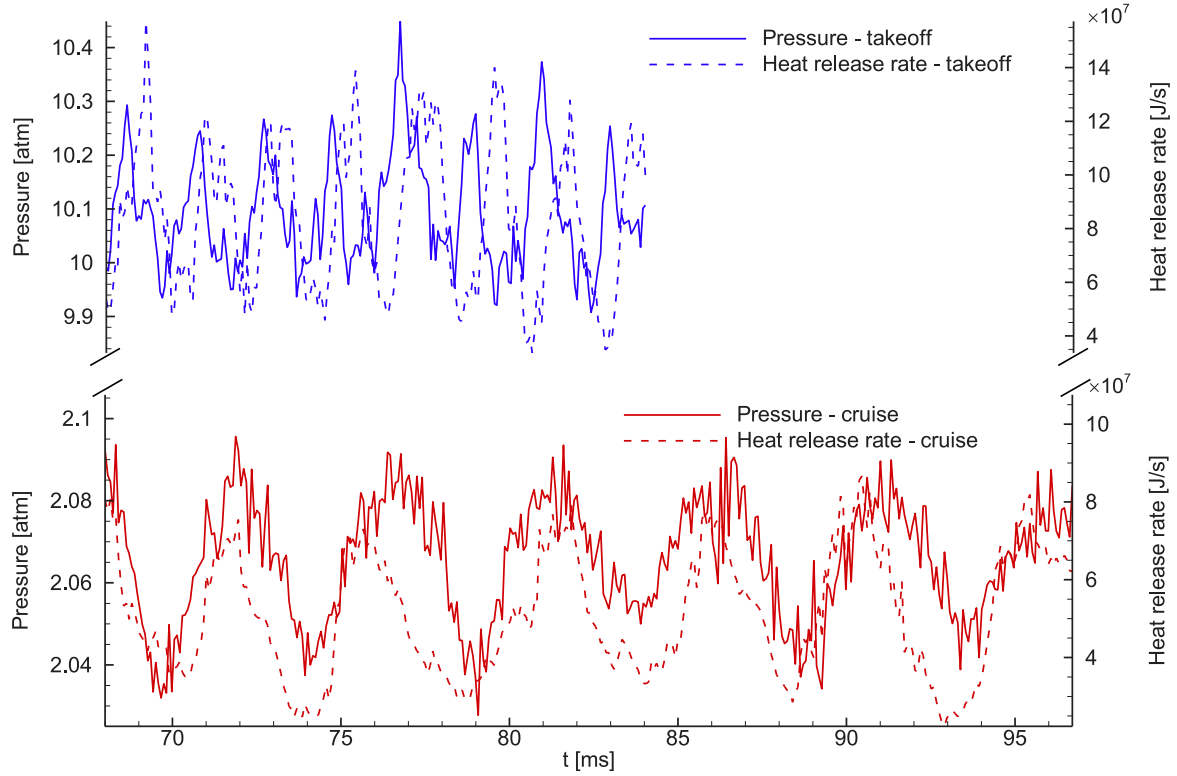
**Fig. 7.** Comparison of pressure and global heat-release signals from LES for the cruise and take-off conditions. The pressure probe is located at the center of the combustor exit plane.
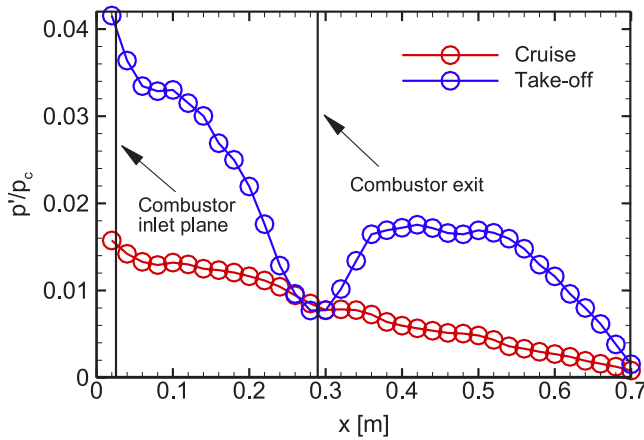


**Fig. 8.** Normalized pressure fluctuation amplitudes of the peak frequency modes along the $x$ axis for the cruise and take-off conditions.

are at maximum a couple percent of the mean effusion flow. Therefore, the liners act almost as a perfectly reflecting boundary, which justifies our constant flow-rate modeling approach.

*Statistical results.* To quantify the effect of the operating condition on the combustor behavior, we present statistical results for pressure, temperature, and mixture fraction. These quantities enter the LEE-model in the form of nozzle-inlet conditions. Statistical results are collected for the duration of six thermoacoustic cycles, corresponding to 24 ms for the cruise condition and 13.2 ms for the take-off condition.

Fig. 11 compares the mean and RMS pressure fields for the cruise and take-off conditions. In this figure, the pressure is normalized by the operating pressure (cruise: 2.07 atm, take-off: 10.35 atm). The normalized mean pressure is shown in Fig. 11(a), and RMS-results are

shown in Fig. 11(b). Overall, the mean pressure field is nearly uniform in the combustion chamber and only decreases in the contraction region before entering the exhaust plenum. Regions of strong pressure fluctuations are observed in Fig. 11(b). Indeed, the high-velocity air-stream supplied by the dilution jets introduces a region of high turbulence and hydrodynamic pressure fluctuations. Furthermore, the volumetric expansion caused by the unsteady heat release generates direct noise that is characterized by broadband pressure fluctuations and a tonal-noise component from the thermoacoustic instability (see Fig. 7). A comparison of the absolute magnitude of the pressure fluctuations shows that the take-off condition results in significantly higher pressure perturbations that exceed those of the cruise condition by an order of magnitude. This is partly due to the higher heat release rate fluctuations $\dot{Q}'$ (shown in Fig. 7) and tonal frequency $f_c$, which will increase the acoustic source term for direct noise $\partial \dot{Q}'/\partial t \propto \dot{Q}' f_c$. Examining the impact of the direct and overall combustion-noise emission will be addressed in Section 4.2.

Fig. 12 compares the mean and RMS temperature fields for the cruise and take-off conditions. These comparisons show qualitative similarities for the mean temperature fields with a more developed flame cone for the take-off condition. Regions of strong temperature fluctuations are visible in the dilution region and near the walls of the secondary combustion zone for the take-off condition. This is attributed to the incomplete combustion and reduced residence time. The swirl-stabilized spray flame generates temperature fluctuations in the shear-layer region but these temperature fluctuations are mostly confined to the primary combustion zone. Considering the temperature field in the secondary zone and at the combustor exit, it can be seen that a thermal boundary layer with relatively high temperature fluctuations forms due to mixing with the effusion cooling.

Fig. 12 also shows the mean and RMS mixture fraction fields for the cruise and take-off conditions. The fuel-rich mixture with $\langle Z \rangle > Z_{st} = 0.064$ is confined to the region near the injector with a larger spatial extent for the take-off condition. The smaller droplets that are injected
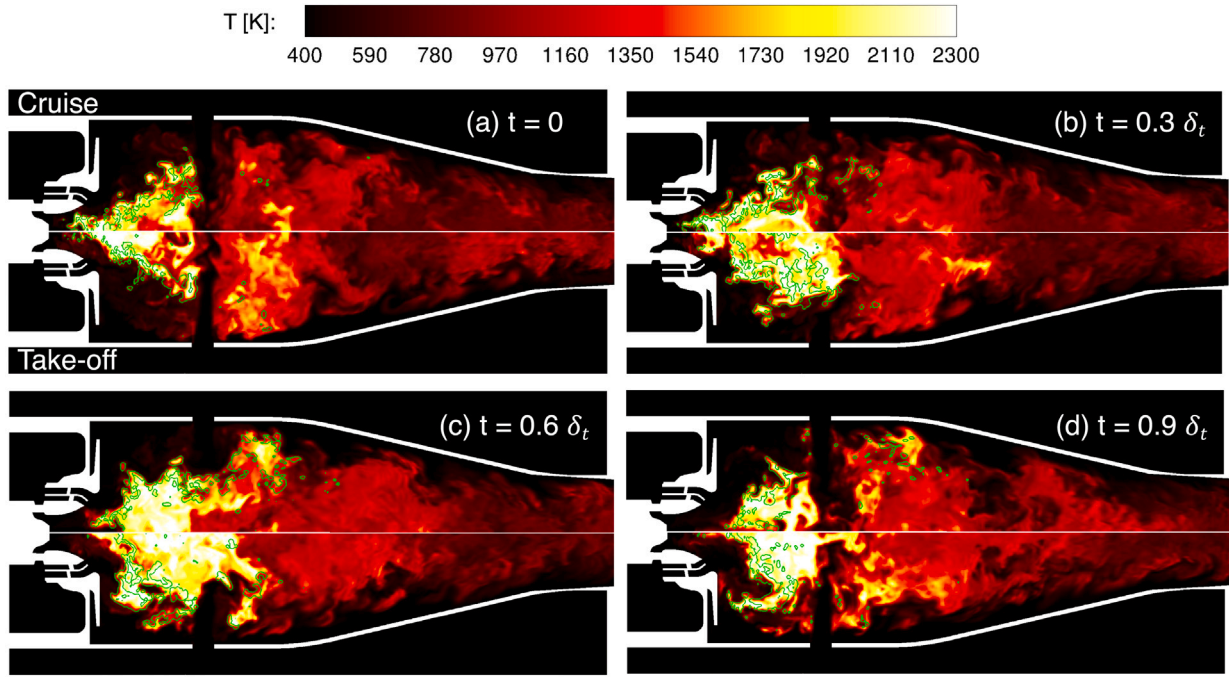
**Fig. 9.** Instantaneous temperature fields in $x$-$y$ plane with isolines of heat release rate (green, $10^9$ W/m$^3$) at four instances during a thermoacoustic cycle for the cruise condition (upper sub-panels) and take-off condition (lower sub-panels): (a) confinement of flame to primary region; (b) hot-spot formation near first dilution holes; (c) convection of hot spots downstream; and (d) dissipation of hot spots by secondary dilution holes and effusive cooling. The cycle period time $\delta_t$ for the cruise and take-off condition is 4.0 ms and 2.2 ms, respectively. (For interpretation of the references to color in this figure legend, the reader is referred to the web version of this article.)
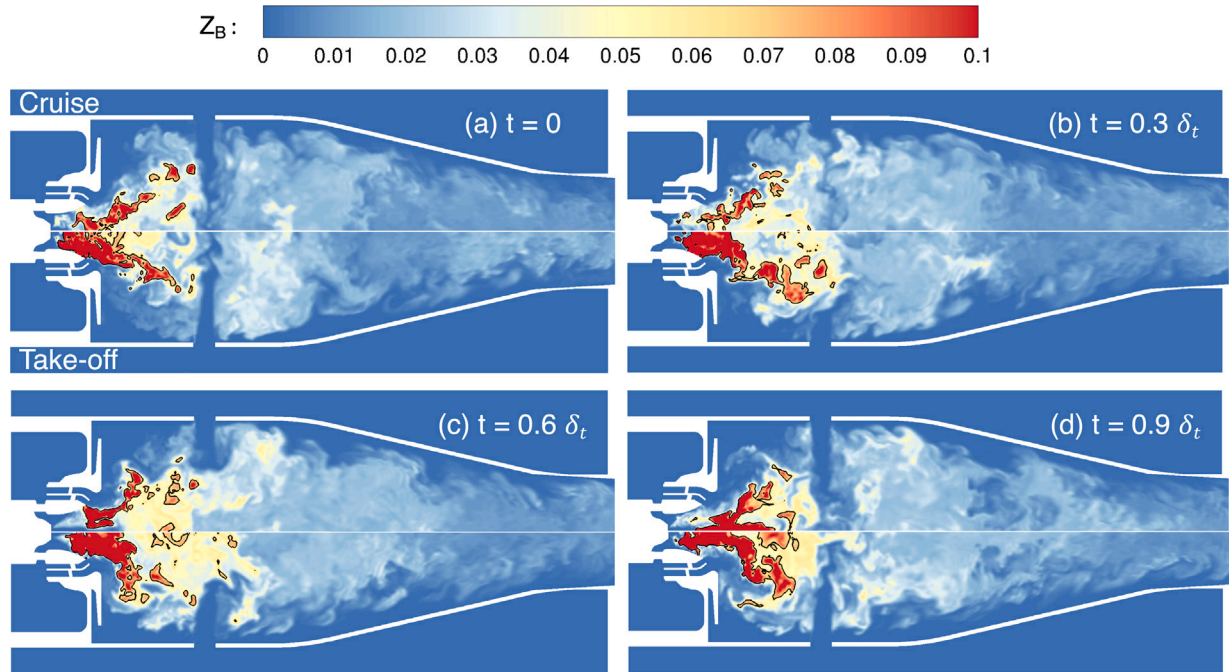


**Fig. 10.** Instantaneous mixture fraction fields in $x$-$y$ plane with isoline of stoichiometric condition (black, $Z_{st} = 0.064$) at four instances during a thermoacoustic cycle for the cruise condition (upper sub-panels) and take-off condition (lower sub-panels). The cycle period time $\delta_t$ for the cruise and take-off condition is 4.0 ms and 2.2 ms, respectively. (For interpretation of the references to color in this figure legend, the reader is referred to the web version of this article.)

for the take-off condition evaporate faster resulting in an extended fuel-rich region. The mixing of the vaporized fuel with the air in the primary zone and by the dilution jets results in a comparable mixing pattern between both operating conditions. Furthermore, it can be seen that the mixture fraction is correlated with the temperature, which is evident from the similarity in temperature and mixture fraction fields at the combustor exit.

*POD analysis.* To prescribe representative boundary conditions for the nozzle flow simulation, we first compute the amplitude spectra for pressure, streamwise velocity, entropy and mixture fraction fluctuations. The mean combustor exit quantities, which are obtained by averaging in time and across the exit area, are used for normalization; these quantities are given as:
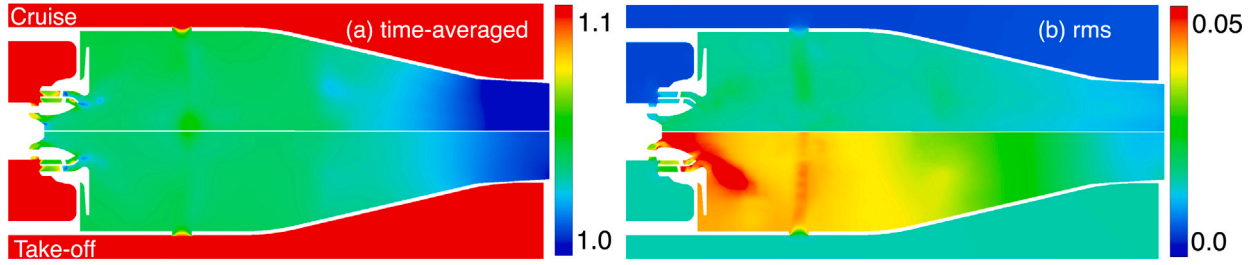
**Fig. 11.** (a) Time-averaged pressure fields and (b) root-mean-square pressure fields for the cruise condition (upper sub-panels) and the take-off condition (lower sub-panels). The pressure is nondimensionalized by the corresponding operating pressure (2.07 atm for the cruise condition and 10.35 atm for the take-off condition).
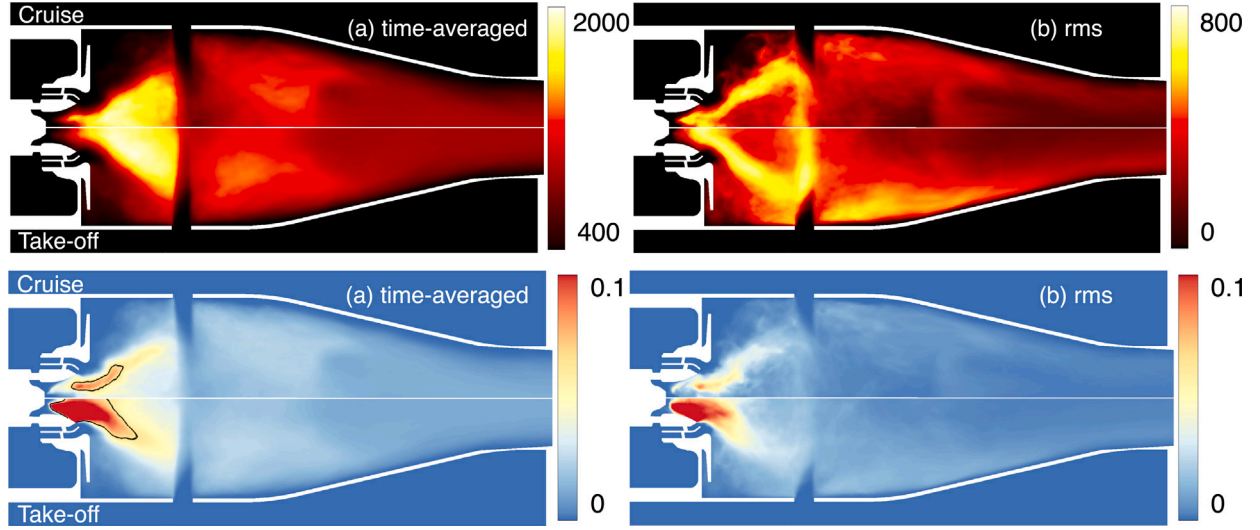


**Fig. 12.** Comparison of (a) time-averaged and (b) root-mean-square temperature fields (top row) and mixture fraction field (bottom row) for the cruise condition (upper sub-panels) and take-off condition (lower sub-panels). The black line represents the stoichiometric mixture fraction iso-line ($Z_{st} = 0.064$). (For interpretation of the references to color in this figure legend, the reader is referred to the web version of this article.)

- Cruise condition: $\langle p \rangle = 2.064$ atm, $\langle u \rangle = 88.2$ m/s, $\langle T \rangle = 898.7$ K, $\langle s \rangle = 3.796$ J/mol/K, $\langle Z \rangle = 0.013$
- Take-off condition: $\langle p \rangle = 10.083$ atm, $\langle u \rangle = 116.1$ m/s, $\langle T \rangle = 940.8$ K, $\langle s \rangle = 3.649$ J/mol/K, $\langle Z \rangle = 0.0134$

Fig. 13 shows the normalized amplitude spectra. The main feature of Fig. 13(a) is that the dominant acoustic frequency for the cruise condition is 254 Hz while the frequency for the take-off condition is shifted to a higher value of 451 Hz.

For the take-off condition, the first and second harmonics are also observed at distinct frequencies (876 Hz, 1344 Hz), leading to a broader acoustic spectrum. Fig. 13(b) shows that the dominant frequencies for velocity fluctuations are correlated to the pressure fluctuations for both conditions, confirming the thermoacoustic nature of the instability. For all fluctuating quantities, the amplitudes at the dominant frequency for the take-off condition are larger than those for the cruise condition. The take-off spectra are also considerably more broadband, and we will analyze in Section 4.2 how this affects indirect noise. It is interesting to observe that the spectral shapes are similar for entropy and mixture fraction fluctuations, which is consistent with the findings observed in Fig. 12.

Fig. 14 shows the first spatial POD mode at the combustor exit for pressure, streamwise velocity, entropy, and mixture fraction fluctuations for both operating conditions. It is interesting to note that the pressure fluctuations are nearly planar for the cruise condition while peaks occur near the wall for the take-off condition. This last result is probably caused by the strong pressure fluctuations observed in the pressure plenum which, in turn, leads to higher pressure fluctuations at the effusive cooling boundaries. For the profiles of the velocity

fluctuations shown in Fig. 14(b), local peaks in the outer region of the boundary layer are observed, which are resulting from the injection of air through the effusive cooling boundaries.

These peak fluctuations also occur in the entropy and mixture fraction profiles at similar locations for the take-off condition but not for the cruise condition, which is an indication of the more intermittent nature of the flow in that region for the former case. This can again be attributed to the effects of effusion cooling.

### 4.2. Combustion-noise analysis

*Thermo-chemical contributions.* To evaluate the strengths of the acoustic sources, we begin our analysis by investigating indirect compositional noise results using one-dimensional counterflow diffusion flames. These calculations are performed using FlameMaster [49]. Profiles of temperature and species mass fractions for the cruise and take-off conditions at scalar dissipation rates of $\chi_{st} = 1\,\mathrm{s}^{-1}$ and $50\,\mathrm{s}^{-1}$ are shown in Fig. 15. The lower dissipation rate is representative of the cruise condition at the combustor exit while the larger value is representative of the take-off condition. Fig. 15 compares the flame structure for both operating conditions, showing similar profiles for temperature and major species. This is in agreement with findings by Sun et al. [66] who investigated the structure of diffusion flames at elevated pressure. The mean composition at the combustor exit is approximately $\langle Z \rangle = 0.013$ and is represented by dashed vertical lines in Fig. 15. For this condition, the mass fractions of the major species ($N_2, O_2, CO_2, H_2O$, CO) amounts to 99.99% of the total composition. Hence, only these species will be used to evaluate the chemical potential function.
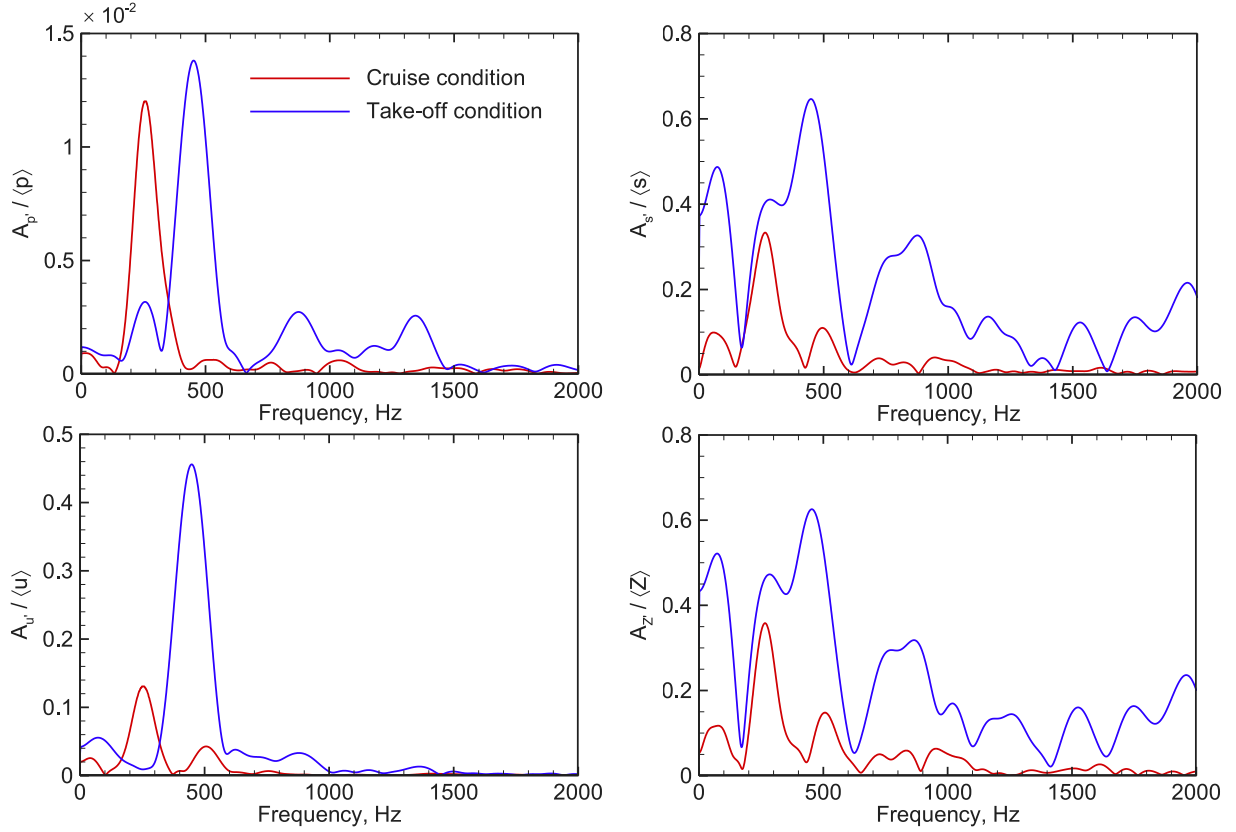
**Fig. 13.** Amplitude spectra for pressure (top-left), entropy (top-right) streamwise velocity (bottom-left) and mixture fraction (bottom-right) fluctuations for the cruise and take-off conditions. The quantities are normalized by the corresponding time-averaged values at the combustor exit.

The noise generation and the transmission through the nozzle are affected by two contributions. One is the perturbation of the flow-field quantities exiting the combustor and entering the nozzle, i.e., $p'$, $u'$, $s'$ and $Z'$. These fluctuations are determined by the combustor operation and can be characterized by their spectra. The second aspect is the mean flow and thermo-chemical properties in the nozzle. The thermo-chemical properties of interest are the heat capacity at constant pressure $c_p$, the ratio of specific heats $\gamma$ and the chemical potential function $\Psi$, which appear in the governing LEE (Eq. (8)).

The quantities $\gamma^{-1}$, $c_p^{-1}$ and $\Psi$, appearing in Eq. (8b), affect the amplitude of the acoustic, entropy and compositional noise contributions [3]. The chemical potential function is calculated from Eq. (10). These quantities are depicted in Fig. 16 as a function of mixture fraction, showing that they are extremely similar between the cruise and take-off conditions. This is attributed to the fact that the composition of the mixture is nearly identical at the combustor exit for these two conditions, suggesting that any indirect noise discrepancy between the cruise and take-off conditions would arise solely from differences at the combustor exit. From Fig. 16, we note that the compositional noise source $\Psi Z'$ has an opposite sign to the entropy noise term, $s'/c_p$, at fuel-lean mixtures. This difference will affect the phase between entropy and compositional noise, and will be further discussed.

We now analyze the quantities affecting the compositional noise. Eq. (10) indicates that it is the difference in Gibbs free energy $g_i$ and the species gradients in mixture fraction space $\partial_Z Y_i$ that induce changes in the chemical potential function and the compositional noise. To understand the sensitivity of the compositional noise to individual species, the contributions of the dominant species to the chemical potential function are examined for three different mixture compositions. The results are presented in Fig. 17, showing that the acoustically most effective species depend on the mixture composition. Specifically,

for lean mixtures that are representative of the present combustor-exit condition, $O_2, H_2O$, and $CO_2$ are the main contributors to the composition noise. However, none of these species contributes to the compositional noise at rich conditions and only $N_2$ has a significant contribution. For the stoichiometric mixture, the intermediate species CO is the main contributor to the chemical potential.

This analysis indicates that the mixture composition requires consideration in the analysis of indirect combustion noise, and measurements of major species ($O_2, H_2O, CO_2$) are useful to guide theoretical analysis.

*Relative importance of combustion-noise sources.* We proceed by examining the relative importance of different core-noise sources. For this, we consider the noise emission at frequencies between 200 and 1400 Hz. The exit-nozzle length is 0.5 m and the Mach number at the nozzle exit is 1.5. Nozzle-inflow conditions are prescribed by a harmonic function $q'(y,t) = \psi_1(y)\sin(2\pi f t + \theta_q)$, where the amplitudes $\psi$ and phase shifts $\theta_q$ are computed from the FFT of signals at the combustor exit. The discrete frequencies considered are $f = \{254, 506, 760, 876, 1000, 1344\}$ Hz for the cruise and take-off conditions.

Sound pressure levels (SPL) for direct and indirect noise emissions at the nozzle exit are presented in Fig. 18. These results show that the total peak sound pressure level is higher by a few decibels at the take-off condition, in accordance with the fluctuating entropy and mixture fraction of higher amplitude (Fig. 14). At higher frequencies, however, the SPL predicted for the take-off condition is up to 20 dB higher compared to the cruise condition for both direct and indirect noise. This can be explained by the results presented in Fig. 13, where take-off fluctuating quantities featured a much higher spectral content above 600 Hz.

With relevance to the relative noise-source contributions, it can be seen that the entropy noise and compositional noise exceed the direct noise at frequencies below 1000 Hz for both conditions. For
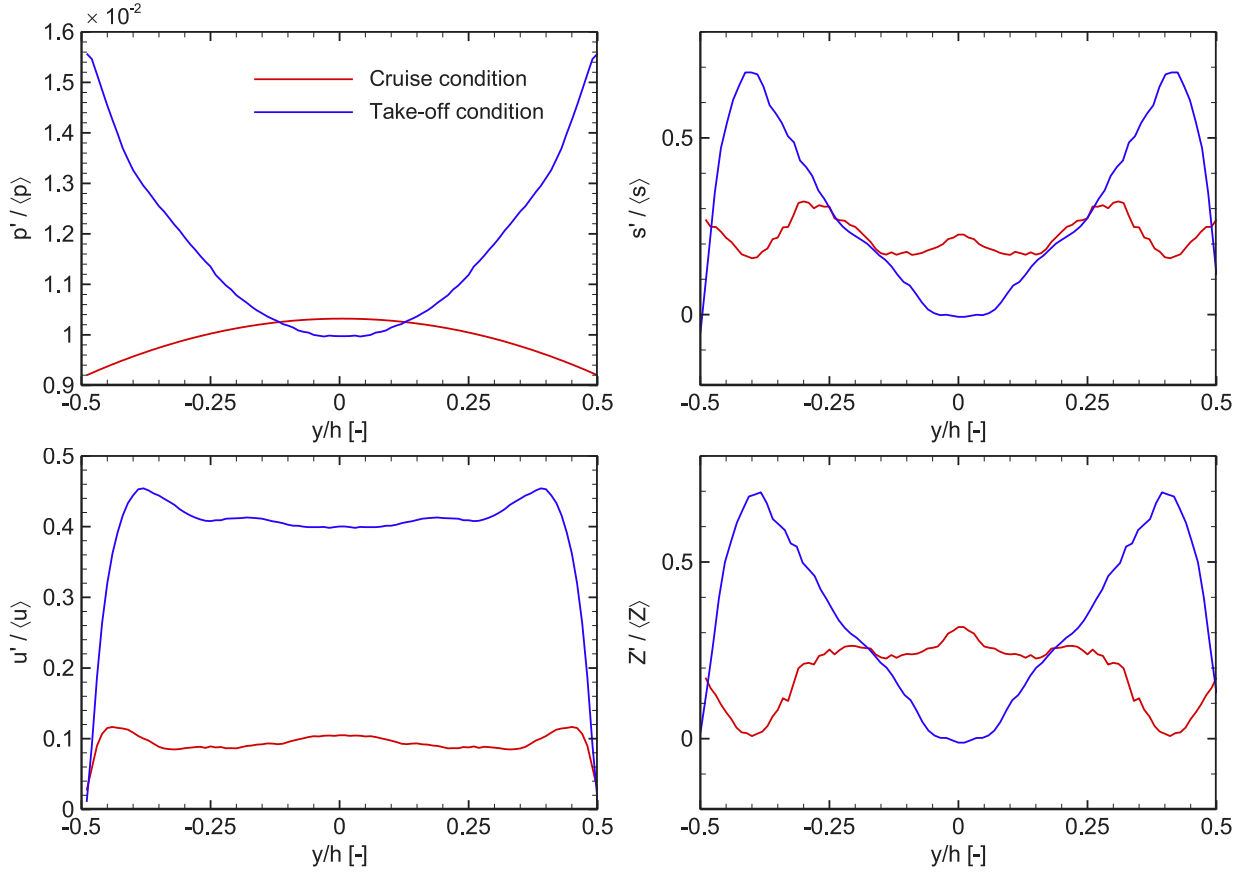
**Fig. 14.** The first spatial POD modes for the pressure, streamwise velocity, entropy and mixture fraction fluctuations for the cruise and take-off conditions. POD modes are obtained from the band-pass filtered LES data at the combustor exit. The quantities are normalized by the corresponding time-averaged values at the combustor exit and $y$ is normalized by the height of combustor exit ($h = 0.052$ m).
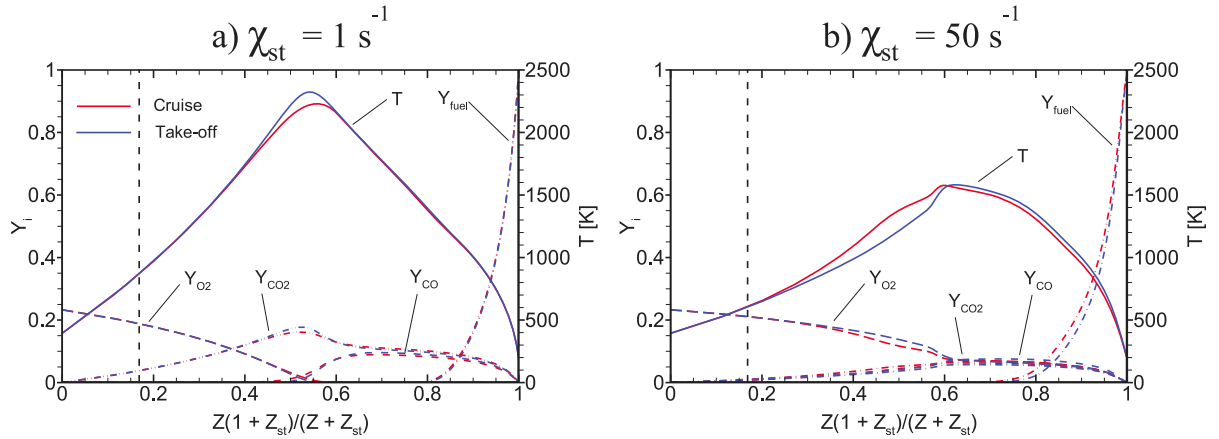


**Fig. 15.** One-dimensional POSF10325-air counterflow diffusion flame quantities for a scalar dissipation rate of (a) $\chi_{st} = 1\,\text{s}^{-1}$ and (b) $\chi_{st} = 50\,\text{s}^{-1}$. The vertical dashed lines indicate the conditions of global equivalence ratio used in this work.

indirect noise, the contribution from compositional noise is 10 dB higher than entropy noise for both conditions. These predictions imply that the compositional noise is the dominant source and entropy noise is secondary for the noise emission. As seen in Fig. 10, the high global equivalence ratio combined with the combustion instability leads to the flame extending downstream the dilution holes and therefore to large mixture fraction fluctuations in that region. This is in contrast with previous results at leaner conditions where the flame is confined to the

primary combustion zone, leading to significantly lower mixture fraction fluctuations at the combustor exit [27]. This explains the higher compositional noise contributions at cruise and take-off conditions.

From the relative contribution of each noise source, we further notice that a phase shift between entropy noise and compositional noise leads to cancellation of indirect noise sources. This is also consistent with previous findings [27] at fuel-lean conditions. Mathematically, this is attributed to the fact that the chemical potential function is
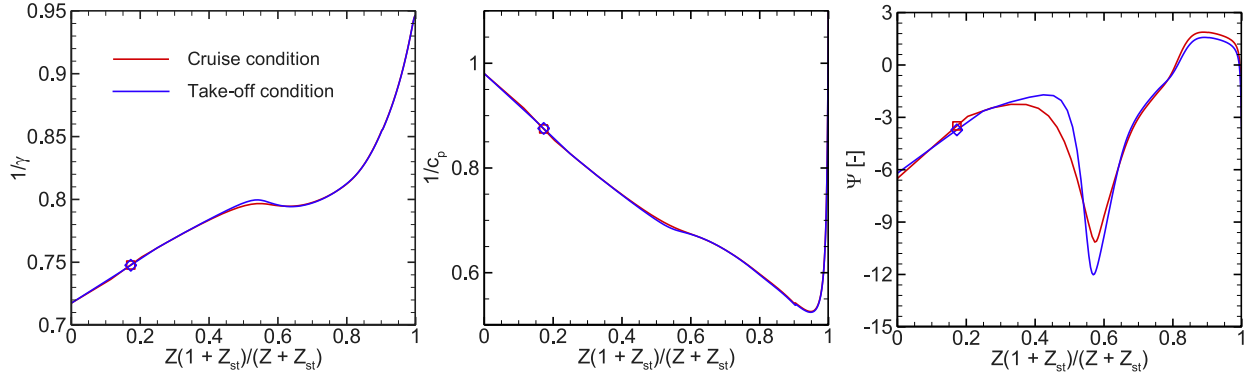
**Fig. 16.** Thermo-chemical quantities (left: heat capacity ratio $\gamma$, center: heat capacity $c_p$, right: chemical potential function $\Psi$) affecting the acoustic, entropy and compositional noise amplitudes, respectively. The symbols represent the conditions of global equivalence ratio used in this work.
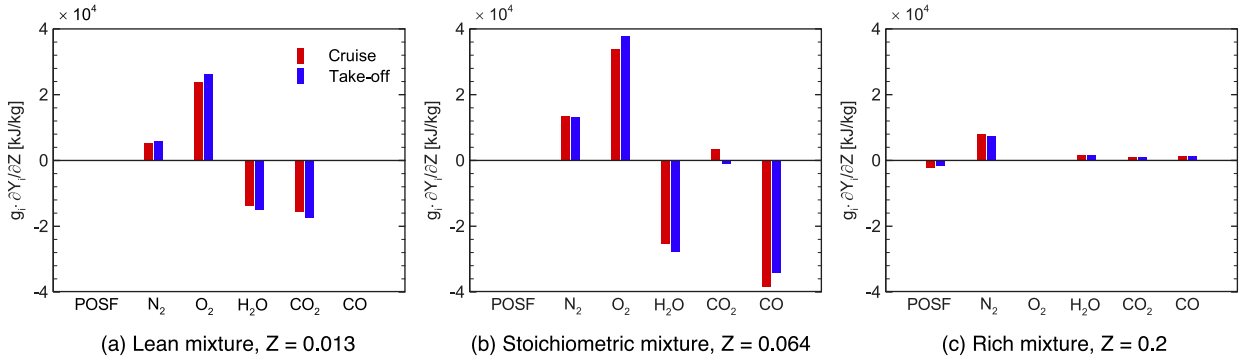


(a) Lean mixture, Z = 0.013
(b) Stoichiometric mixture, Z = 0.064
(c) Rich mixture, Z = 0.2

**Fig. 17.** Contribution of the dominant species to the chemical potential function, $\Psi$, i.e., $g_i \partial Y_i / \partial Z$ at different mean mixture fraction, where the lean mixture corresponds to the present combustor-exit condition.
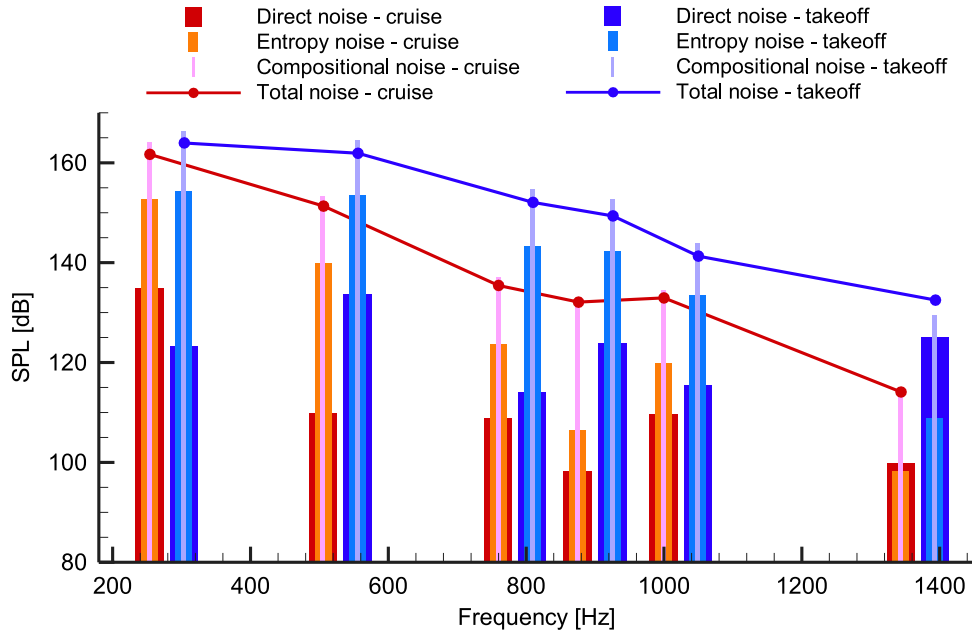


**Fig. 18.** Sound pressure levels for direct and indirect noises predicted by the LEE simulations for the cruise (red lines) and take-off (blue lines) conditions. (For interpretation of the references to color in this figure legend, the reader is referred to the web version of this article.)

negative for fuel lean mixture, which is of opposite sign compared to the entropy noise source term, as shown in Fig. 16.

*Low-order modeling of combustion noise.* We further assess the correlation between pressure fluctuation and mass flow rate by considering the
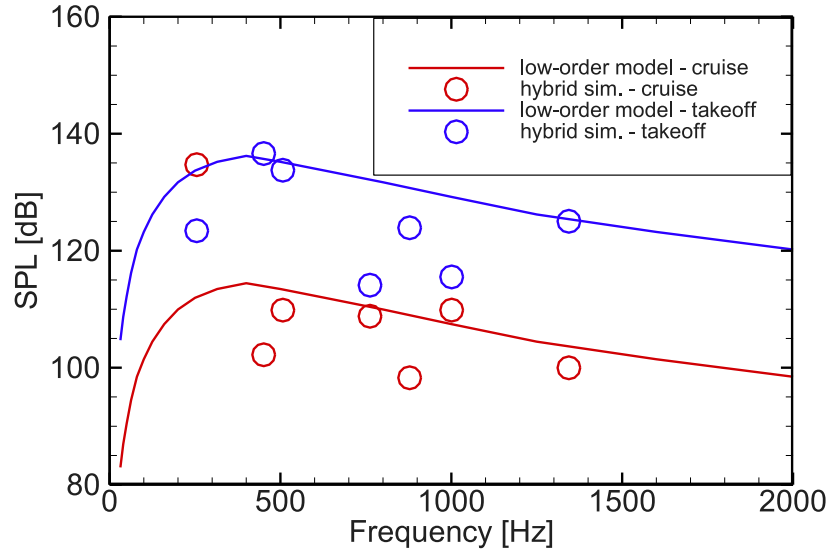
**Fig. 19.** Comparison of the low-order combustion noise model with the hybrid modeling results [67] for the cruise and take-off conditions.

Aircraft Noise Prediction Program (ANOPP) model [67]. In this model, the acoustic power is expressed as

$$\Pi = 10^{K/10} a_\infty^2 \dot{m}_C \left( \frac{T_{t4} - T_{t3}}{T_{t3}} \right)^2 \left( \frac{p_{t3}}{p_\infty} \right)^2 \times F_{TA}, \tag{12}$$

where $K = -60.53$ is a constant, $a_\infty$ is the ambient speed of sound, $\dot{m}_C$ is the mass flow rate through the combustor, $T_{t4}$ and $T_{t3}$ are the temperature at combustor exit and inlet, respectively, $p_{t3}$ is the combustor-inlet pressure, $p_\infty$ is the ambient pressure, and $F_{TA}$ is the turbine attenuation/loss factor which is set to unity in this work. The overall power level (OAPWL) can further be expressed as OAPWL = $10 \log_{10} \left( \Pi / \Pi_{ref} \right)$, where $\Pi_{ref} = 1 \times 10^{-12}$ W. The spectral shape that correlates $\Delta dB \sim f$ is obtained from [68] where the peak frequency is 400 Hz. The comparison of the combustion model and the simulation results for both conditions are shown in Fig. 19. This comparison shows that the low-order model is in overall good agreement with the results obtained from the hybrid model for both conditions. Given the empirical nature and calibration of this low-order model from global engine properties, this agreement is encouraging. This model was specifically developed for predicting broadband combustion noise, and is not able to reproduce the dominant frequency of the combustion instability that was predicted by the hybrid model. While some discrepancies might arise from certain modeling assumptions made in the hybrid LES/LEE methodology, which should be developed towards a more comprehensive approach in the future, this comparison illustrates the utility of the hybrid model towards assessing low-order models and adapting these models to current engine configurations and operating regimes.

## 5. Conclusions

In this study, we presented and applied a simulation framework for enabling noise-prediction analysis, suitable for application to realistic gas-turbine combustor flow path configurations. This hybrid modeling approach, which is a step towards a full-core engine simulation, combines LES for the prediction of the unsteady turbulent combustion with a linearized Euler formulation for the prediction of the noise generation through the downstream flow path. The generation and transmission of direct and indirect noise was investigated and the relative importance of noise sources for two distinct thermo-acoustically unstable operating points were examined. From the present study, the following conclusions can be drawn:

- Large fluctuations in pressure, temperature and mixture fraction at the combustor exit originated from the thermo-acoustic instability. Mixing with the dilution jets decreased the fluctuation levels but still resulted in inhomogeneous combustor-exit conditions.
- Higher levels of fluctuation were found at the take-off condition compared to the cruise condition. Specifically, higher pressure fluctuations were due to an increased fuel flow rate and thermo-acoustic frequency.
- The relative contributions in fluctuations in species composition and temperature were comparable for cruise and take-off conditions. Analogously, the relative levels of the direct and indirect noise contributions remained the same for the present combustor configuration.
- The direct and indirect combustion noise were up to 20 dB higher for the take-off condition at frequencies above 600 Hz, and the compositional noise exceeded the temperature-induced entropy noise.
- The species $O_2$, $H_2O$, $N_2$ and $CO_2$ were the primary contributors to the indirect noise arising from mixture inhomogeneities at fuel-lean conditions, suggesting that further measurements of these quantities can provide further diagnostics on the importance of compositional noise.
- The entropy and compositional noise contributions partially canceled due to the opposite signs of the heat capacity ratio and the chemical potential function at fuel-lean conditions.
- The low-order modeling was in overall good agreement with the results obtained from the hybrid model for the cruise and take-off conditions.

The hybrid LES/LEE method was demonstrated to be an effective approach for predicting the core noise for the combustor-nozzle configuration. The actual configuration of the turbine stage, in particular the turbine-inlet guide vanes, should be considered in future work. The feedback effect of direct and indirect noise should also be considered, as it could change the combustor dynamics and the relative balance between the noise components. The flexibility of the hybrid method enables extensions of these computational studies to other combustor configurations and operating conditions, which is required to assess the generalization of the conclusions from this study.

**Table B.3**

Parameters of the nozzle geometry for a nozzle length $L = 0.5$ m ($x_t$ is the throat location, $A_{a/b}$ is the inlet/outlet area, $M_{a/b}$ is the inlet/outlet Mach number, $T_{a/b}$ is the inlet/outlet temperature, $p_{a/b}$ is the inlet/outlet pressure, and $Z_{a/b}$ is the inlet/outlet mixture fraction).

| | $x_t$ [m] | $A_a$ [cm$^2$] | $A_b$ [cm$^2$] | $M_a$ [–] | $M_b$ [–] | $T_a$ [K] | $T_b$ [K] | $p_a$ [atm] | $p_b$ [atm] | $Z_{a/b}$ [–] |
|---|---|---|---|---|---|---|---|---|---|---|
| Cruise | 0.35 | 58.76 | 17.67 | 0.15 | 1.5 | 898.7 | 622.6 | 2.06 | 0.55 | 0.013 |
| Take-off | 0.34 | 58.76 | 17.53 | 0.19 | 1.5 | 940.8 | 653.5 | 10.08 | 2.82 | 0.0134 |

## Funding sources

## Declaration of competing interest

The authors declare that they have no known competing financial interests or personal relationships that could have appeared to influence the work reported in this paper.

## Acknowledgments

## Appendix A. Parametric cycle analysis of turbofan engine

We consider a turbofan engine in this work, consisting of a fan, compressor, combustor, turbine and nozzle. The operating parameters for the specific conditions considered (take-off and cruise) are then obtained from an engine-cycle analysis [39], given the inputs on flight Mach number $M_0$, ambient temperature $T_\infty$, heat capacity ratio $\gamma$, heat capacity $c_p$, lower heating value $\Delta h_f^0$, temperature at the combustor exit $T_{t4}$, compressor pressure ratio $\pi_c$, fan pressure ratio $\pi_f$, and bypass ratio $\beta$:

$$a_\infty = \sqrt{\gamma R T_\infty}, \tag{A.1a}$$

$$\tau_r = 1 + \frac{\gamma - 1}{2} M_0^2, \tag{A.1b}$$

$$\tau_\lambda = \frac{T_{t4}}{T_\infty}, \tag{A.1c}$$

$$\tau_c = \pi_c^{\frac{(\gamma-1)}{\gamma}}, \tag{A.1d}$$

$$\tau_f = \pi_f^{\frac{\gamma-1}{\gamma}}, \tag{A.1e}$$

$$\frac{V_9}{c_0} = \sqrt{\frac{2}{\gamma - 1} \left\{ \tau_\lambda - \tau_r \left[ \tau_c - 1 + \beta \left( \tau_f - 1 \right) \right] - \frac{\tau_\lambda}{\tau_r \tau_c} \right\}}, \tag{A.1f}$$

$$\frac{V_{19}}{c_0} = \sqrt{\frac{2}{\gamma - 1} \left( \tau_r \tau_f - 1 \right)}, \tag{A.1g}$$

$$\frac{F}{\dot{m}_0} = c_0 \frac{1}{1 + \beta} \left[ \frac{V_9}{c_0} - M_0 + \beta \left( \frac{V_{19}}{c_0} - M_0 \right) \right], \tag{A.1h}$$

$$f_r = \frac{c_p T_0}{\Delta h_f^0} \left( \tau_\lambda - \tau_r \tau_c \right), \tag{A.1i}$$

$$TSFC = \frac{f_r}{(1 + \beta) \left( F/\dot{m}_0 \right)}, \tag{A.1j}$$

where $R$ is the gas constant, $a_\infty$ is the ambient speed of sound, $\tau_r$ is total/static temperature ratio in the free stream, $\tau_\lambda$ is the ratio of the burner exit enthalpy to the ambient enthalpy, $\tau_c$ is the compressor temperature ratio, $\tau_f$ is the fan temperature ratio, $V_9$ is the velocity at the nozzle exit, $V_{19}$ is the velocity at the fan exit, $\dot{m}_0$ is the total air mass flow rate, $F/\dot{m}_0$ is the specific thrust, $f_r$ is the fuel–air ratio, and $TSFC$ is the thrust specific fuel consumption.

## Appendix B. Nozzle geometry

We consider the isentropic nozzle in this work, where the nozzle cross-section area $A$, pressure $p$, and temperature $T$ along the nozzle can be calculated as:

$$\frac{A}{A_*} = \frac{1}{M} \left[ \left( \frac{2}{\gamma + 1} \right) \left( 1 + \frac{\gamma - 1}{2} M^2 \right) \right]^{\frac{\gamma+1}{2(\gamma-1)}}, \tag{B.1a}$$

$$\frac{p}{p_*} = \left( 1 + \frac{\gamma - 1}{2} M^2 \right)^{\frac{-\gamma}{\gamma-1}}, \tag{B.1b}$$

$$\frac{T}{T_*} = \left( 1 + \frac{\gamma - 1}{2} M^2 \right)^{-1}, \tag{B.1c}$$

where the subscript $*$ denotes the throat location. The quantities at the throat location can be determined based on the nozzle inlet quantities and these equations. We summarize the quantities at the nozzle inlet (denoted as $a$) and nozzle outlet (denoted as $b$) in Table B.3.

## References

[1] Basner M, Clark C, Hansell A, Hileman JI, Janssen S, Shepherd K, Sparrow V. Aviation noise impacts: State of the science. Noise Health 2017;19:41–50.

[2] ICAO. Icao circular 333: Global air transport outlook to 2030 and trends to 2040. 2013.

[3] Ihme M. Combustion and engine-core noise. Annu Rev Fluid Mech 2017;49:277–310.

[4] Chang CT, Lee C-M, Herbon JT, Kramer SK. NASA Environmentally responsible aviation project develops next-generation low-emissions combustor technologies (Phase I). J Aeronaut Aerospace Eng 2013;2:1000116.

[5] Lieuwen T, Zinn BT. The role of equivalence ratio oscillations in driving combustion instabilities in low nox gas turbines. In: Symposium (international) on combustion, vol. 27, 1998, pp. 1809–1816.

[6] Liu Y, Dowling A, Swaminathan N, Morvant R, Macquisten M, Caracciolo L. Prediction of combustion noise for an aeroengine combustor. J Propul Power 2013;30:114–22.

[7] Dowling AP, Mahmoudi Y. Combustion noise. In: Proc. combust. inst. vol. 35, 2015, pp. 65–100.

[8] Moreau S. Turbomachinery noise predictions: Present and future. Acoustics 2019;1:92–116.

[9] Pillai A, Kurose R. Combustion noise analysis of a turbulent spray flame using a hybrid DNS/APE-RF approach. Combust Flame 2018;200:168–91.

[10] Pausch K, Herff S, Nawroth H, Paschereit CO, Schröder W. Noise sources of a lean-premixed jet flame. In: AIAA Paper 2018, 2018–4088.

[11] Candel S, Durox D, Ducruix S, Birbaud A-L, Noiray N, Schuller T. Flame dynamics and combustion noise: progress and challenges. Int J Aeroacoustics 2009;8:1–56.

[12] Marble FE, Candel SM. Acoustic disturbance from gas non-uniformities convected through a nozzle. J Sound Vib 1977;55:225–43.

[13] Magri L, O'Brien J, Ihme M. Compositional inhomogeneities as a source of indirect combustion noise. J Fluid Mech 2016;799:R4.

[14] Bake F, Richter C, Mühlbauer C, Kings N, Röhle I, Thiele F, Noll B. The entropy wave generator (EWG): A reference case on entropy noise. J Sound Vib 2009;326:574–98.

[15] Rolland EO, De Domenico F, Hochgreb S. Direct and indirect noise generated by entropic and compositional inhomogeneities. J Eng Gas Turb Power 2018;140:082604.

[16] Cumpsty NA, Marble FE. Core noise from gas turbine exhausts. J Sound Vib 1977;54:297–309.

[17] Stow SR, Dowling AP, Hynes TP. Reflection of circumferential modes in a choked nozzle. J Fluid Mech 2002;467:215–39.

[18] Goh CS, Morgans AS. Phase prediction of the response of choked nozzles to entropy and acoustic disturbances. J Sound Vib 2011;330:5184–98.

[19] Duran I, Moreau S. Solution of the quasi-one-dimensional linearized euler equations using flow invariants and the Magnus expansion. J Fluid Mech 2013;723:190–231.

[20] Duran I, Morgans AS. On the reflection and transmission of circumferential waves through nozzles. J Fluid Mech 2015;773:137–53.

[21] Huet M, Giauque A. A nonlinear model for indirect combustion noise through a compact nozzle. J Fluid Mech 2013;733:268–301.

[22] Leyko M, Nicoud F, Poinsot T. Comparison of direct and indirect combustion noise mechanisms in a model combustor. AIAA J 2009;47:2709–16.

[23] Papadogiannis D, Wang G, Moreau S, Duchaine F, Gicquel L, Nicoud F. Assessment of the indirect combustion noise generated in a transonic high-pressure turbine stage. J Eng Gas Turb Power 2016;138:1–8.

[24] O'Brien J, Kim J, Ihme M. Integrated analysis of jet-engine core noise using a hybrid modeling approach. In: AIAA Paper 2015, 2015–2821.

[25] Livebardon T, Moreau S, Gicquel L, Poinsot T, Bouty E. Combining les of combustion chamber and an actuator disk theory to predict combustion noise in a helicopter engine. Combust Flame 2016;165:272–87.

[26] Magri L, O'Brien J, Ihme M. Effects of nozzle Helmholtz number on indirect combustion noise by compositional perturbations. J Eng Gas Turb Power 2018;140:1–9.

[27] Shao C, Maeda K, Ihme M. Analysis of core-noise contributions in a realistic gas-turbine combustor operated near lean blow-out. Proc Combust Inst 2021;38:6203–11.

[28] Stouffer S, Hendershott T, Monfort JR, Diemer J, Corporan E, Wrzesinski P, Caswell AW. Lean blowout and ignition characteristics of conventional and surrogate fuels measured in a swirl stabilized combustor. In: AIAA Paper 2017, 2017–1954.

[29] Colket M, Heyne J, Rumizen M, Gupta M, Edwards T, Roquemore WM, Andac G, Boehm R, Lovett J, Williams R, et al. Overview of the national jet fuels combustion program. AIAA J 2017;55:1087–104.

[30] Esclapez L, Ma PC, Mayhew E, Xu R, Stouffer S, Lee T, Wang H, Ihme M. Fuel effects on lean blowout in a realistic gas turbine combustor. Combust Flame 2017;181:82–99.

[31] Colket M, Heyne J. Fuel effects on operability of aircraft gas turbine combustors. In: Progress in astronautics and aeronautics AIAA. 2021, p. 262.

[32] Hasti VR, Kundu P, Kumar G, Drennan SA, Som S, Won SH, Dryer FL, Gore JP. Lean blow-out (lbo) computations in a gas turbine combustor. In: AIAA Paper 2018, 2018–4958.

[33] Panchal A, Ranjan R, Menon S. Effect of chemistry modeling on flame stabilization of a swirl spray combustor. In: AIAA Paper 2018, 2018–4684.

[34] Outcalt S, Laesecke A, Freund MB. Density and speed of sound measurements of jet A and S-8 aviation turbine fuels. Energ Fuels 2009;23:1626–33.

[35] Coordinating Research Council, Inc. Handbook of aviation fuel properties. Warrendale, PA: Society of Automotive Engineers, Inc.; 1983.

[36] Jenkinson L, Simpkin P, Rhodes D. Civil Jet Aircraft Design. American Institute of Aeronautics and Astronautics; 1999.

[37] Commercial aircraft propulsion and energy systems research: reducing global carbon emissions. National Academies Press; 2016.

[38] Monfort JR, Stouffer S, Hendershott T, Wrzesinski P, Foley W, Rein KD. Evaluating combustion instability in a swirl-stabilized combustor using simultaneous pressure, temperature, and chemiluminescense measurements at high repetition rates. In: AIAA Paper 2017, 2017–1101.

[39] Mattingly JD, Boyer KM. Elements of propulsion: gas turbines and rockets. 2nd ed. American Institute of Aeronautics and Astronautics; 2016.

[40] El-Sayed AF. Aircraft propulsion and gas turbine engines. CRC Press; 2008.

[41] Khalighi Y, Nichols JW, Ham F, Lele SK, Moin P. Unstructured large eddy simulation for prediction of noise issued from turbulent jets in various configurations. In: AIAA Paper 2011, 2011–2886.

[42] Ma PC, Lv Y, Ihme M. An entropy-stable hybrid scheme for simulations of transcritical real-fluid flows. J Comput Phys 2017;340:330–57.

[43] Wu H, Ma PC, Jaravel T, Ihme M. Pareto-efficient combustion modeling for improved CO-emission prediction in LES of a piloted turbulent dimethyl ether jet flame. Proc Combust Inst 2019;37:2267–76.

[44] Gottlieb S, Shu CW, Tadmor E. Strong stability-preserving high-order time discretization methods. SIAM Rev 2001;43:89–112.

[45] Wu H, Ma PC, Ihme M. Efficient time-stepping techniques for simulating turbulent reactive flows with stiff chemistry. Comput Phys Comm 2019;243:81–96.

[46] Vreman AW. An eddy-viscosity subgrid-scale model for turbulent shear flow: Algebraic theory and applications. Phys Fluids 2004;16:3670–81.

[47] Pierce CD, Moin P. Progress-variable approach for large-eddy simulation of non-premixed turbulent combustion. J Fluid Mech 2004;504:73–97.

[48] Ihme M, Cha CM, Pitsch H. Prediction of local extinction and re-ignition effects in non-premixed turbulent combustion using a flamelet/progress variable approach. Proc Combust Inst 2005;30:793–800.

[49] Pitsch H. FlameMaster v3.1: A C++ computer program for 0D combustion and 1D laminar flame calculations. 1998.

[50] Wang H, Xu R, Wang K, Bowman CT, Davidson DF, Hanson RK, Brezinsky K, Egolfopoulos FN. A physics-based approach to modeling real-fuel combustion chemistry - I. Evidence from experiments, and thermodynamic, chemical kinetic and statistical considerations. Combust Flame 2018;193:502–19.

[51] Ihme M, Shunn L, Zhang J. Regularization of reaction progress variable for application to flamelet-based combustion models. J Comput Phys 2012;231:7715–21.

[52] Moin P, Apte SV. Large-eddy simulation of realistic gas turbine combustors. AIAA J 2006;44(4):698–708.

[53] Miller RS, Harstad KG, Bellan J. Direct numerical simulations of supercritical fluid mixing layers applied to heptane-nitrogen. J Fluid Mech 2001;436:1–39.

[54] Apte SV, Gorokhovski M, Moin P. LES of atomizing spray with stochastic modeling of secondary breakup. Int J Multiph Flow 2003;29:1503–22.

[55] Lefebvre AH. Atomization and sprays. In: Hemisphere. 1989.

[56] Holmes P, Lumley JL, Berkooz G, Rowley CW. Turbulence, coherent structures, dynamical systems, and symmetry. Cambridge: Cambridge University Press; 2012.

[57] Bogey C, Bailly C. A family of low dispersive and low dissipative explicit schemes for flow and noise computations. J Comput Phys 2004;194(1):194–214.

[58] Freund JB. Proposed inflow/outflow boundary condition for direct computation of aerodynamic sound. AIAA J 1997;35:740–2.

[59] Poinsot TJ, Lele SK. Boundary conditions for direct simulations of compressible viscous flows. J Comput Phys 1992;101:104–29.

[60] Rock N, Stouffer SD, Hendershott TH, Corporan E, Wrzesinski P. Characterization of coherent flow structures in a swirl-stabilized spray combustor. In: AIAA Paper 2021, 2021–0791.

[61] Bokhart AJ, Shin D, Gejji R, Buschhagen T, Naik SV, Lucht RP, Gore JP, Sojka P, Meyer SE. Spray measurements at elevated pressures and temperatures using phase Doppler anemometry. In: AIAA Paper 2017, 2017–0828.

[62] Sattelmayer T. Influence of the combustor aerodynamics on combustion instabilities from equivalence ratio fluctuations. J Eng Gas Turb Power 2003;125:11–9.

[63] Bilger RW. The structure of diffusion flames. Combust Sci Tech 1976;13:155–70.

[64] Dassé J, Mendez S, Nicoud F. Large-Eddy Simulation of the acoustic response of a perforated plate. In: AIAA Paper 2008, 2008–3007.

[65] Howe MS. On the theory of unsteady high Reynolds number flow through a circular aperture. Proc R Soc Lond Ser A Math Phys Eng Sci 1979;366:205–23.

[66] Sun CJ, Sung CJ, Zhu DL, Law CK. Response of counterflow premixed and diffusion flames to strain rate variations at reduced and elevated pressures. Symp (Int) Combust 1996;26(1):1111–20.

[67] Hultgren L. A comparison of combustor-noise models. In: AIAA Paper 2012, 2012–2087.

[68] Ho P, Doyle V. Combustion noise prediction update. In: AIAA Paper 1979, 1979–588.